Paris $N\bar{N}$ potential and recent proton-antiproton low energy data

M. Pignone,[1] M. Lacombe,[2] B. Loiseau,[2] and R. Vinh Mau[2]
[1]*Istituto Nazionale di Fisica Nucleare, Sezione di Torino, 10125 Torino, Italy*
[2]*Division de Physique Théorique, Institut de Physique Nucléaire, 91406 Orsay Cedex, France and LPTPE, Université Pierre et Marie Curie, 4 Place Jussieu, 75252 Paris Cedex 05, France*
(Received 5 August 1994)

The inner part of the Paris nucleon-antinucleon optical potential has been reanalyzed in view of new experimental constraints. These are mainly provided by accurate measurements of the analyzing power in charge-exchange scattering, $\bar{p}p \to \bar{n}n$, together with elastic $\bar{p}p \to \bar{p}p$ polarization data, allowing a better determination of the isospin dependence of the short-range forces. The fit is performed with a set of 3632 data. The good quality of the fit is illustrated over a large sample of observables for laboratory momenta from 180 to 910 MeV/c. Curves of the potentials and of the phase shifts are shown as well as the parameters of the potentials and effective range formula coefficients for the S and P waves. The spectrum of resonances and bound states predicted by our potential is also displayed. In particular, a bound state having the $AX(1565)$ quantum numbers is found with the right mass.

PACS number(s): 13.75.Cs, 21.30.+y

I. INTRODUCTION

In 1982 we proposed an optical potential for the description of the low energy nucleon-antinucleon ($N\bar{N}$) interaction [1]. The real part of this optical potential is obtained by G-parity transformation of the theoretical long- and medium-range (LR+MR) parts of the Paris NN potential, supplemented with a phenomenological short-range (SR) part. Its absorptive part has a form suggested by detailed calculations of the $N\bar{N}$ annihilation diagrams into two mesons or resonances; in particular, it is of short range, energy and state dependent. The parameters of the short-range potentials, both real and imaginary, were determined by fitting to the world data set of that time, which consisted of total and elastic cross sections [2–9], and of few elastic polarization data at two energies [10,11]. For the charge-exchange reaction, the only data were some total [12,13] and differential cross sections [4,13,14]. The fit we performed at that time required an isospin dependence for the SR potential, although its accurate determination was not possible. It led to a χ^2/data of 2.80 for 915 data points.

During the last decade, many new and accurate measurements have been performed at different laboratories not only on differential cross sections but also on analyzing power for elastic and charge-exchange scatterings. These data provide additional constraints for the determination of the model, which was so far essentially constrained by the $\bar{p}p$ elastic data, i.e., in the isospin ($T = 1 + T = 0$) combination. The new charge-exchange data provide now constraints on the orthogonal ($T = 1 - T = 0$) combination, and this allows a determination of the isospin dependence.

In the present work we supersede the phenomenological short-range part of the $N\bar{N}$ optical model considered in Ref. [1] by readjusting the parameters to fit the existing set of experimental results in the range of kinetic energies $17 < T_{\rm lab} < 370$ MeV.

This paper is organized as follows. In Sec. II we recall the principal features of our model and we describe the procedure for the determination of the parameters. The results on elastic and charge-exchange scatterings and on total and annihilation cross sections are presented and discussed in Sec. III. In the same section the obtained $N\bar{N}$ optical potential is displayed as well as the phase shifts for low angular momentum ($J \leq 2$), and S- and P-wave low energy parameters are tabulated. Predictions on $N\bar{N}$ resonances and bound states are also presented there. A summary and conclusions are given in Sec. IV. The detailed expressions and the parameters of our optical potential are shown in the Appendix.

II. THE MODEL

A. Basic considerations

As stated in the Introduction, the model considered in this work is essentially based on the same theoretical and phenomenological considerations as in Ref. [1]. The $N\bar{N}$ interaction is described by an optical potential

$$V_{N\bar{N}} = U_{N\bar{N}} - iW_{N\bar{N}}. \tag{2.1}$$

In principle, the real part $U_{N\bar{N}}$ can be obtained by the G-parity transform of the NN potential if this is due to meson exchanges. For large and medium distances between the nucleons ($r \geq r_c = 1$ fm), it is well established that meson exchanges provide a very good description of the NN forces. We therefore take the real part $U_{N\bar{N}}$, for these distances between the nucleon and antinucleon ($r \geq 1$ fm), as strictly given by the G-parity transform of the theoretical Paris NN potential. This means that it contains, besides the one-pion exchange,

the two-pion (correlated and uncorrelated) exchange and the ω and A_1 meson exchanges as parts of the three-pion exchange. For small distances ($r < 1$ fm), other degrees of freedom (e.g., quarks, gluons) come into play and, at present, there exists no reliable theoretical account for these. Thus one is forced provisionally to content oneself with a phenomenological description for this region. This is the attitude we adopted for the Paris NN potential and we do the same here. Now, one should remember that the spin and isospin structure of the $N\bar{N}$ interaction requires the presence, for each isospin state, of five independent invariants with *five* radial potentials. Moreover, for the distances of interest here ($r < 1$ fm), these radial potentials are expected to be nonlocal, meaning that these five radial potentials are functions of two variables. We could have transposed to the present work the very simple procedure we used successfully in the NN case [15]. (i) To cut off the theoretical potential at $r = 1$ fm and replace each radial potential by a constant for $r < 1$ fm. This introduces five parameters representing the heights of the radial potentials for the inner regions. (ii) To implement nonlocality only in the central components via a linear p^2 or energy dependence. This adds two other parameters.

Thus, even in this ultrasimple parametrization, this requires in total seven parameters, and we believe that this is a *minimum minimorum*. To facilitate the numerical calculations, we are using here a slightly different procedure. For small distances $r < 1$ fm, we expand the phenomenological radial potentials in powers of r [Eqs. (A4) and (A5)] and match them to the theoretical ones at two points in the vicinity of 1 fm. In this way, we also preserve entirely the theoretical potential for interdistances larger than 1 fm. This procedure leaves us with nine parameters instead of seven as discussed above. The two extra parameters arise from the cubic expansion of the central potentials [Eq. (A4)].

The imaginary part $W_{N\bar{N}}$ takes into account the $N\bar{N}$ annihilation into mesons and can be calculated from annihilation diagrams, as represented in Fig. 1, which reflect nothing else but the unitary condition (see the Appendix). Since the nucleon and antinucleon annihilate mostly into four or five pions, the dominant diagram is that with this number of pions in the intermediate state. This diagram is quite difficult to calculate. However, in the approximation [16] where the annihilation into four or five pions proceeds through annihilation into two mesons (π, ϵ, ρ, or ω mesons), the calculation of $W_{N\bar{N}}$, still complicated, becomes possible (see again the Appendix). It can be seen from Fig. 1 that the annihilation diagrams imply the exchange of a baryon-antibaryon pair in the t channel. The resulting $W_{N\bar{N}}$ is of short range and nonlocal, i.e., again with five radial potentials of two variables for each isospin. As discussed in the Appendix, our minimal model contains, for each isospin, six parameters, i.e., the strengths of the different spin-dependent components and a linear energy dependence for the central components that accounts for a minimum nonlocality.

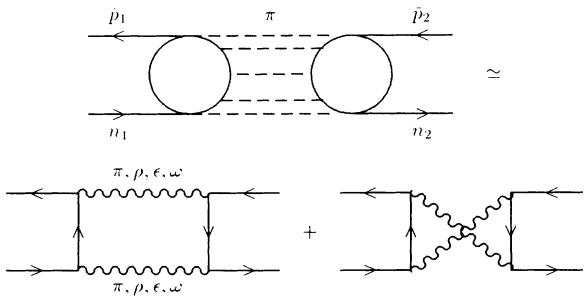

FIG. 1. $N\bar{N}$ annihilation diagrams.

B. Determination of the short-range parameters

In total, the model contains, for each isospin state, 15 parameters. Because of this number, superficial considerations may lead one to conclude that the model could be simply a "numerical recipe" [17]. From our general analysis, we believe that this is a *minimal* model if, in the $N\bar{N}$ system, one wishes to take into account the simultaneous presence of scattering and annihilation processes and the complex spin and isospin structure. There exists no good reason to discard *a priori* any of the general features represented by this set of parameters. Only a detailed analysis can allow us to reduce this number of parameters.

Of course, these 15 parameters do not play an equal role in the fitting procedure. Actually, we start the search by setting, for $r < r_c$, all potentials except the central to zero, and then introduce progressively the tensor and spin-orbit components. In this process, we found that the "weighty" parameters are (i) for the real part, the six parameters giving the heights of the central triplet and singlet, of the tensor, and of the LS components at $r = r_2 = 0.6$ fm; (ii) for the imaginary part, the four couplings of the triplet and singlet central components. The remaining five parameters allow just a fine tuning of the fit.

III. RESULTS

A. Elastic scattering: $\bar{p}p \to \bar{p}p$

1. *Differential cross sections*

In general, the elastic differential cross sections [2–6,18–24] are well reproduced as can be seen in Figs. 2 and 3. A quantitative statement on the fit, in terms of a χ^2 value, is more delicate as there are, for several energies, inconsistencies between different sets of experimental data.

For example, around $T_{\rm lab} = 225$ MeV ($P_{\rm lab} = 688$ MeV/c), there are three recent sets of data, of Kunne *et al.* [22] (at 220 MeV, $60° \leq \theta \leq 120°$), of Bertini *et al.* [23] (at 230.6 MeV, $36° \leq \theta \leq 163°$), and of Kageyama *et al.* [24] (at 225.8 MeV, $22° \leq \theta \leq 167°$) along with three earlier sets of Iwasaki *et al.* [25] (at 224.1 MeV,

$3° \leq \theta \leq 20°$), of Eisenhandler *et al.* [5] (at 226.4 MeV, $22° \leq \theta \leq 162°$), and of Kaseno *et al.* [26] (at 230.5 MeV, $8° \leq \theta \leq 31°$). Disagreement between Kageyama *et al.* and Eisenhandler *et al.* data for small angles ($20° - 40°$) has been noticed long ago [24]. Those of Kageyama *et al.* are lower and compatible with the results of Bertini *et al.* in this region but they are significantly higher than the data of Bertini *et al.* and Kunne *et al.* for large angles ($80° - 120°$) with a maximum discrepancy around $95° - 100°$. Beyond 120°, they are significantly lower

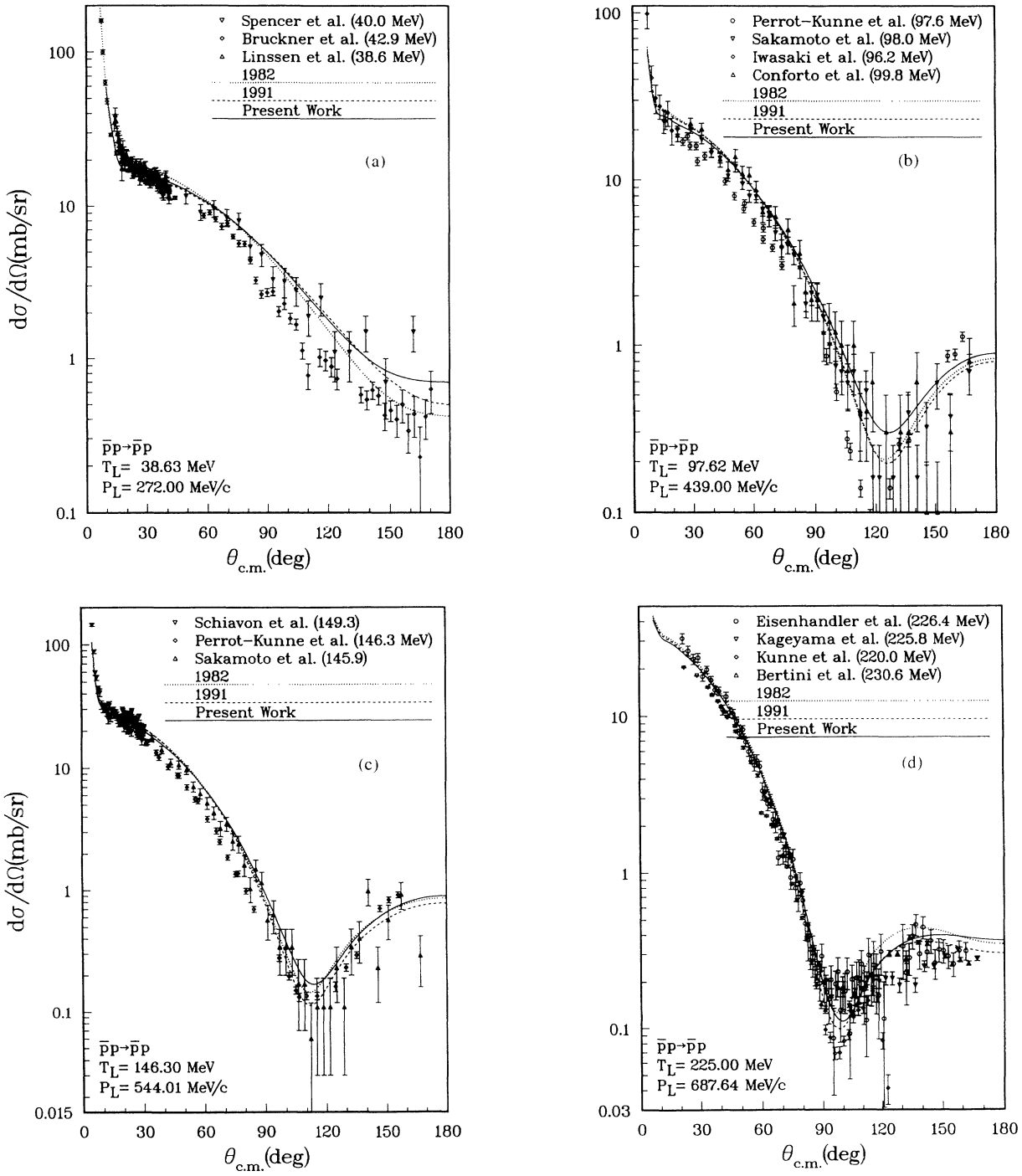

FIG. 2. Elastic differential cross sections for different values of T_L ($= T_{\text{lab}}$). Curves labeled 1982 and 1991 are from our works of Refs. [1] and [17], respectively. Data are from Conforto *et al.* [2], Eisenhandler *et al.* [5], Linssen *et al.* [18], Schiavon *et al.* [19], Brückner *et al.* [20], Perrot-Kunne *et al.* [21], Kunne *et al.* [22], Bertini *et al.* [23], Kageyama *et al.* [24], Iwasaki *et al.* [25], Kaseno *et al.* [26], and Sakamoto *et al.* [27].

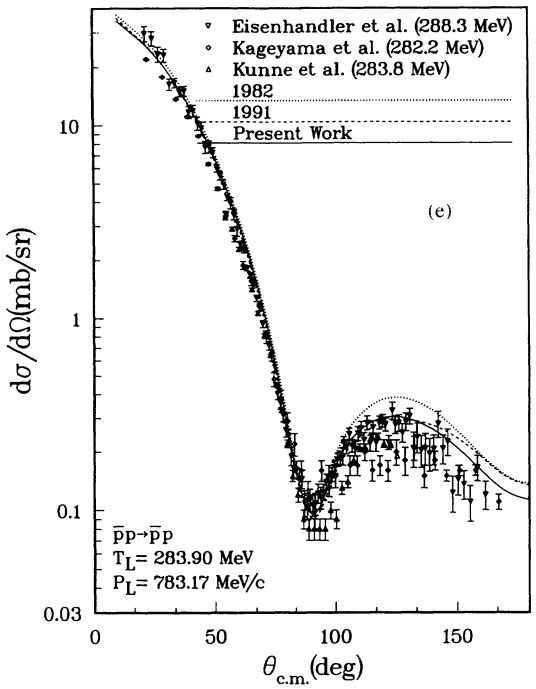

FIG. 2. (*Continued*).

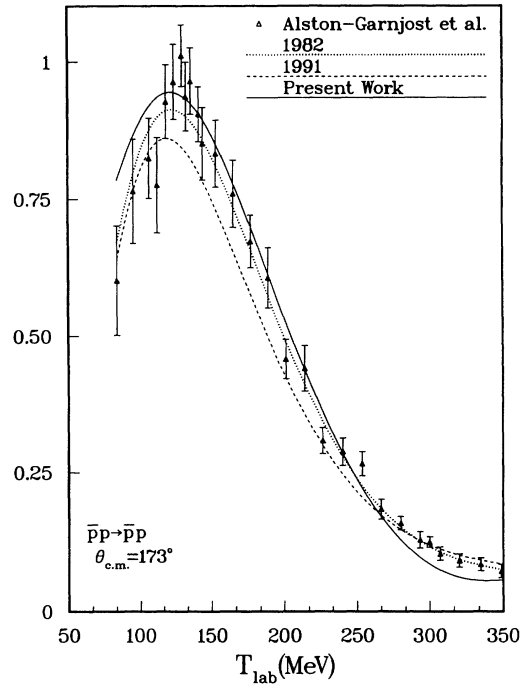

FIG. 3. Backward elastic differential cross sections for different values of T_L. Curves are as in Fig. 2. Data are from Alston-Garnjost *et al.* [6].

than those of Bertini *et al.* The two sets converge, however, near 170° towards the results of Alston-Garnjost *et al.* [6]. The Kunne *et al.* data, except the two last points, can be reconciled with those of Bertini *et al.* by a slight renormalization. The Eisenhandler *et al.* data with larger errors bars can also be reconciled with the other sets except with those of Kageyama *et al.* near the forward angles. All these features are summarized in Fig. 2. Note that in all the figures no renormalization factor has been used. Finally, the data of Kaseno *et al.* and of Iwasaki *et al.*, at small angles, are compatible with those of Eisenhandler *et al.* because of their large error bars but they are higher than those of Kageyama *et al.* Such a situation requires a selection of the data for the determination of the model parameters. We decided not to retain those of Kageyama *et al.* In these conditions, it is not surprising that they will contribute a large amount to the χ^2 for the total data set.

In the energy domain around 225 MeV, the results are as follows. For the set of Kunne *et al.*, we get χ^2/data=9.2 (for 21 data) with, however, a sizable renormalization (1.48); this value was obtained without taking into account the two first values and the two last ones which are obviously spurious. In general, the data of Kunne *et al.* require a rather large renormalization. It is 1.30 at 283.9 MeV and 1.20 at 352.3 MeV. For the set of Bertini *et al.*, we obtain a χ^2/data = 16 (for 23 data) with, however, a significantly weaker renormalization (1.13). For the set of Kageyama *et al.*, χ^2/data = 18.3 (for 38 data) with a renormalization of 1.17. Finally, for the sets of Iwasaki *et al.*, Eisenhandler *et al.*, and Kaseno *et al.*, the χ^2/data values are 1.02 (for eight data), 2.49 (for 88 data), and 1.1 (for 15 data), respectively, with the corresponding normalization of 0.95, 1.03, and 0.95.

At other energies, the largest contributions to χ^2/data come from the data of Kageyama *et al.* The most unfavorable case is for 120.24 MeV where the fit is good for small angles (30° – 60°) but not so good for angles between 80° and 130°. In this case, normalization cannot help. The data of Perrot-Kunne *et al.* [21] at 97.62 MeV give rise to a significant χ^2/data. They appear to be too

TABLE I. χ^2/data on differential elastic cross sections.

Elastic $d\sigma/d\Omega$	Number of data points	χ^2/data
Pre-LEAR [2–5,25–29]	2414	1.64
LEAR at forward angles [18,19]	237	1.75
LEAR at non forward angles [20–23]	337	17.74
KEK [24] (not used in the fit)	168	25.21
Complete set of data	3156	4.63

low and, despite a normalization factor of 1.5, the value for χ^2/data is still as high as 68 (for 26 data). However, their four data from 105° to 117° are outside the uncertainties of Conforto *et al.* [2] and Sakamoto *et al.* [27]. If these points are removed, the χ^2/data drops to 22. Moreover, the last three points from 156° to 163° are hardly compatible with the results of Alston-Garnjost *et al.* [6] at 173° and with those of Conforto *et al.* and Sakamoto *et al.* If, in addition, we eliminate these three points, we get χ^2/data = 14. It should be noted that at 146.3 MeV and 105° $\leq \theta \leq$ 116°, there is no such disagreement between Perrot-Kunne *et al.* and Conforto

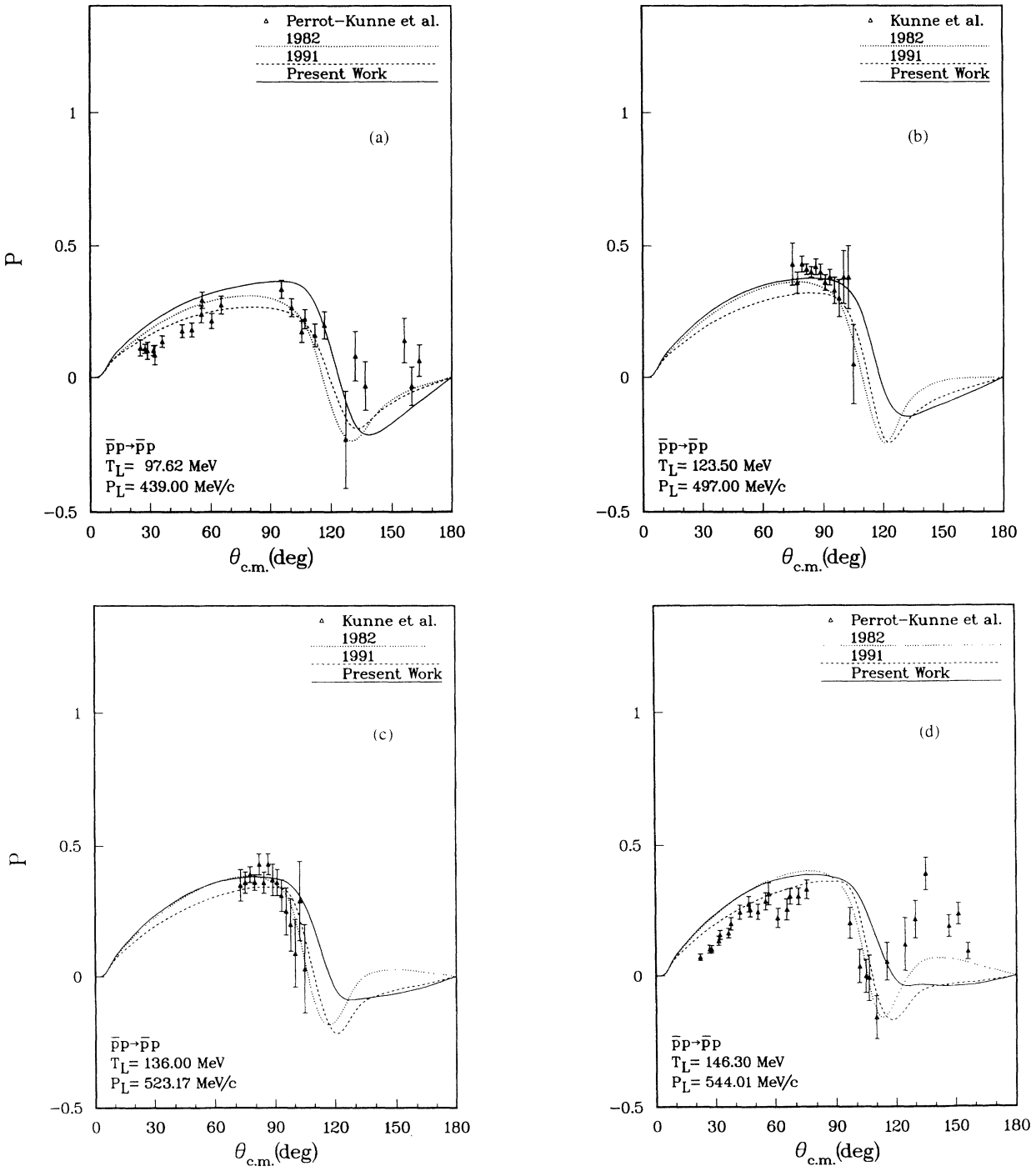

FIG. 4. Elastic polarizations for different values of T_L. Curves are as in Fig. 2. Data are from Oshugi *et al.* [10], Perrot-Kunne *et al.* [21], Kunne *et al.* [22], and Bertini *et al.* [23].

et al. and Sakamoto *et al.* The fit is then automatically better, 43 (for 32 data) against 68. Finally, the backward differential cross-section measurements of Alston-Garnjost *et al.* [6] which were, in 1982, among the most constraining and useful data, due to their high precision, are still well reproduced (Fig. 3). The present χ^2/data on elastic differential cross sections are summarized in Table I. The high values obtained with the LEAR and KEK differential cross sections reflect inconsistencies in these data and disagreements with the pre-LEAR measurements [2–5,25–29].

2. *Polarization*

In 1982, below 350 MeV the set of experimental data on polarization was very scarce. There were only four points at 220 and 232 MeV [10,11] at forward angles. During the period 1988–1991, many more accurate measurements for various angles in the range of 20° to 170°

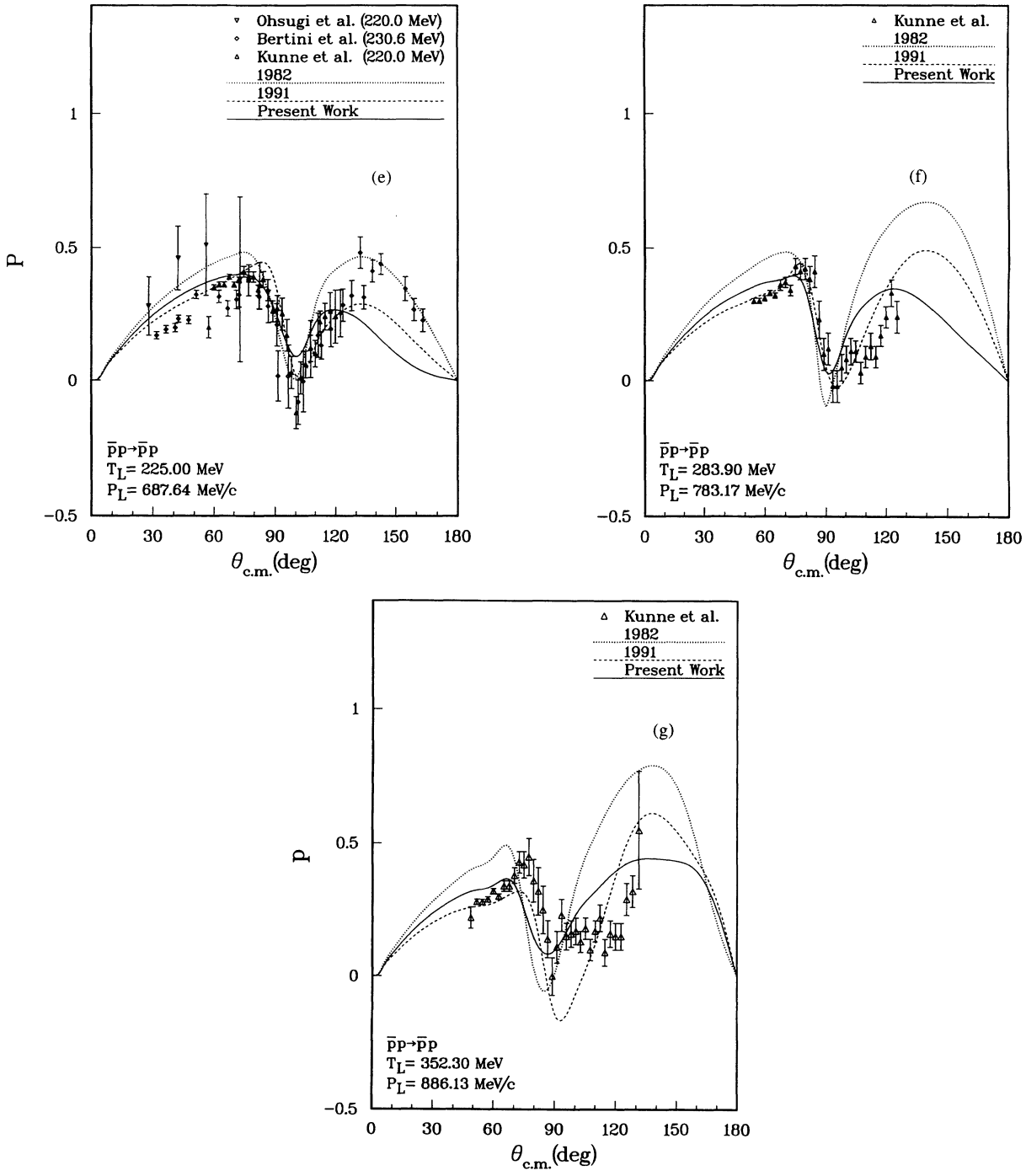

FIG. 4. (*Continued*).

were performed at LEAR [21–23]. In Fig. 4, we give the results obtained with the present model and comparison is made with those of Refs. [1] and [30]. The angular dependence of the polarization is well reproduced by our model but, in order to achieve a good fit, some renormalization of the data is required, especially for those of Perrot-Kunne *et al.* [21]. As no definite number was stated in these references, we assumed a normalization error of 5% and then obtain, for the whole set of data, χ^2/data of 6.25 for 219 data.

B. Charge-exchange reaction $\bar{p}p \to \bar{n}n$

In 1984, new measurements of charge-exchange (CEX) differential cross sections [31,32] showed that the model

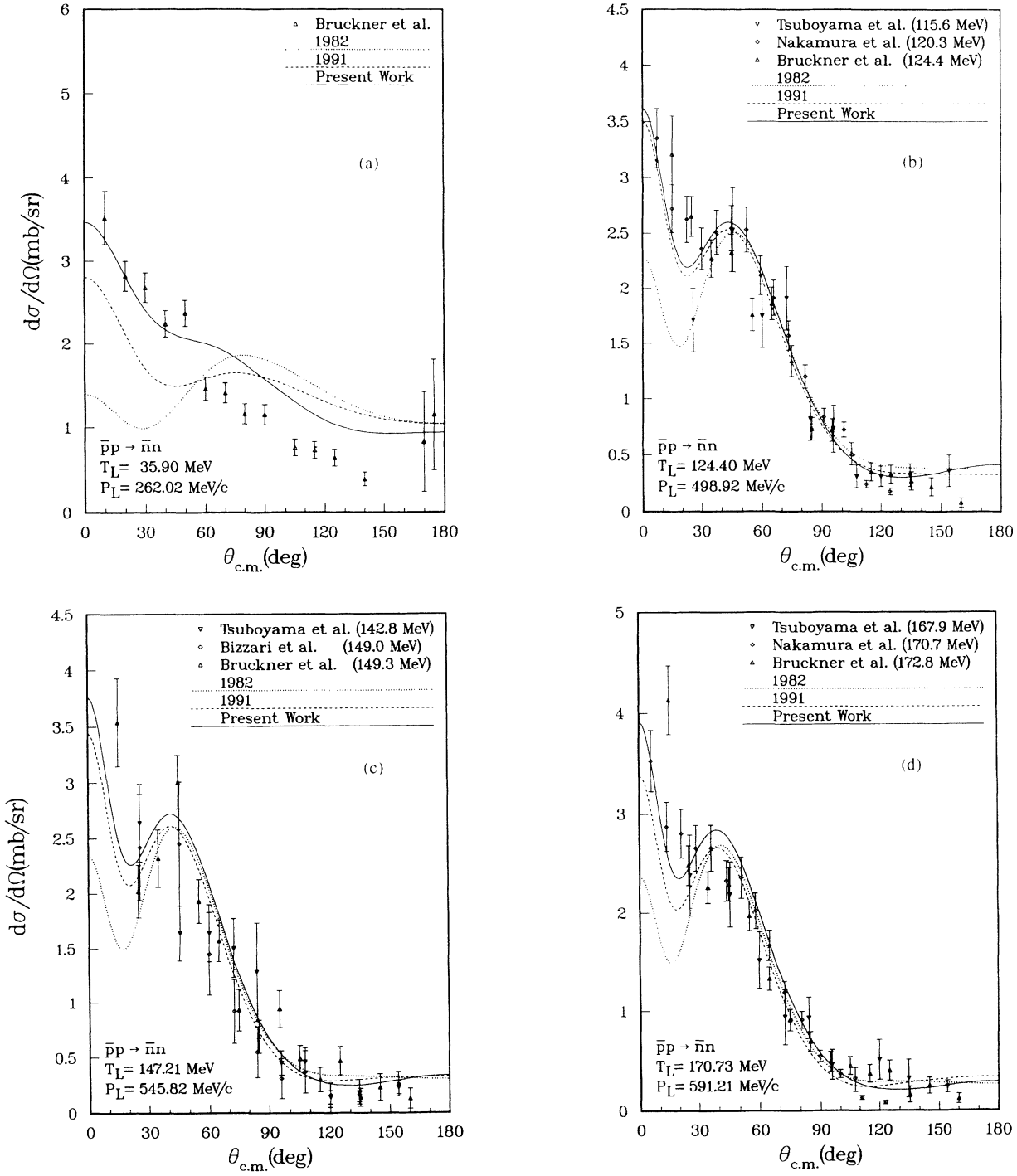

FIG. 5. Charge-exchange differential cross sections for different values of T_L. Curves are as in Fig. 2. Data are from Kohno *et al.* [4], Tsuboyama *et al.* [13], Bizzari *et al.* [14], Nakamura *et al.* [31], Brückner *et al.* [32], and Birsa *et al.* [33].

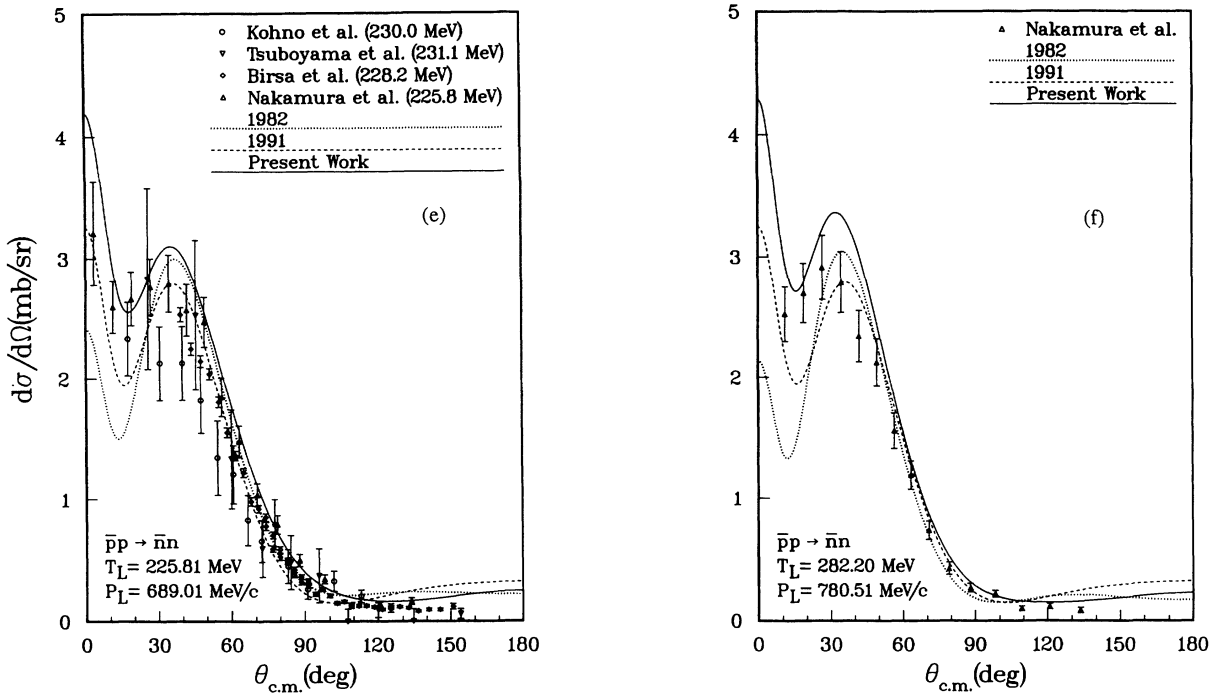

FIG. 5. (*Continued*).

of Ref. [1] predicts a too pronounced dip in the forward direction (see Fig. 5). In Ref. [30] it is shown that the discrepancies for the CEX differential cross sections in the forward directions can be eliminated and, at the same time, the fit to elastic scattering observables (differential cross sections and analyzing power) improved by readjusting only the SR parameters. However, in 1990, preliminary results [33] on a new observable, namely, the CEX analyzing power at $T_{\rm lab} = 206.6$ MeV ($P_{\rm lab} = 656$ MeV/c), show again a disagreement between the data and the predictions of Ref. [30]. This disagreement was confirmed by subsequent measurements at different energies [34], (see Fig. 6). At this point, the important question was whether or not one can amend the situation by acting once more on the SR part of the potential. The following results show a positive answer. Actually, we realized quickly that the CEX analyzing power is very sensitive to the SR potential. We first try to get a good fit of this observable even at the expense of spoiling the good agreement for CEX cross sections and elastic scattering data. Then we make a fine tuning on the SR parameters to restore this good agreement. The results are shown in Fig. 6.

1. *Differential cross section*

In this case, even for the very low energies, the improvement of the fit with respect to the original solution of Ref. [1] is quite significant at forward angles, $\theta < 90°$ (see Fig. 5). Here again, when the comparison between the results of different experiments [4,13–33] can be done, we note some disagreements which cannot be easily solved by a renormalization of the data. This is true at backward angles for $T_{\rm lab} = 124.4$ MeV [Fig. 5(b)] and $T_{\rm lab} = 170.7$ MeV [Fig. 5(d)]. Anyway, despite an improvement with respect to the previous solution, it remains difficult to fit the data below $T_{\rm lab} = 50$ MeV. For the whole set of 331 data with $17.3 \leq T_{\rm lab} \leq 282.2$ MeV we obtain χ^2/data of 6.13. If we exclude the 71 data below 50 MeV, it drops to 3.56.

2. *Polarization*

Here also the improvement with respect to previous solutions is noticeable, especially at angles less than 90° (Fig. 6). The present model, for 85 data ($147.2 \leq T_{\rm lab} \leq 344.5$ MeV) [34], gives χ^2/data of 3.62. When we try to obtain a best fit to these polarizations alone, the other data are still correctly reproduced, except for the CEX differential cross sections which come out too large even though their shapes are correct. This indicates either inconsistencies between these data or underestimated errors for some of them. Incidently, the new LEAR experiment (PS206) planned for further studies of the CEX reaction is very welcome.

3. *Depolarization*

This parameter has been measured for the first time at LEAR at $T_{\rm lab} = 344.7$ MeV ($P_{\rm lab} = 875$ MeV/c) [35]. The components of the scattering amplitude, appearing in the expression for the depolarization, are complemen-

tary to those of the analyzing power. Moreover, these components are linked, at least in the Born approximation, to the spin-spin and tensor. This implies a particular sensitivity to the LR and MR parts of the interaction. Thus, although the error bars remain large, the remarkable agreement between data and predictions of our model confirms the validity of the LR and MR meson exchange forces for the $\bar{N}N$ system (Fig. 7).

C. Total and annihilation cross sections

The total and annihilation cross sections predicted by our model are shown in Figs. 8(a) and 8(b). The $\bar{p}p$ total cross sections [7,36–38] are well reproduced. For the annihilation process [39–41], our results are too low. The $\bar{n}p$ system, which is pure $T = 1$, is interesting for

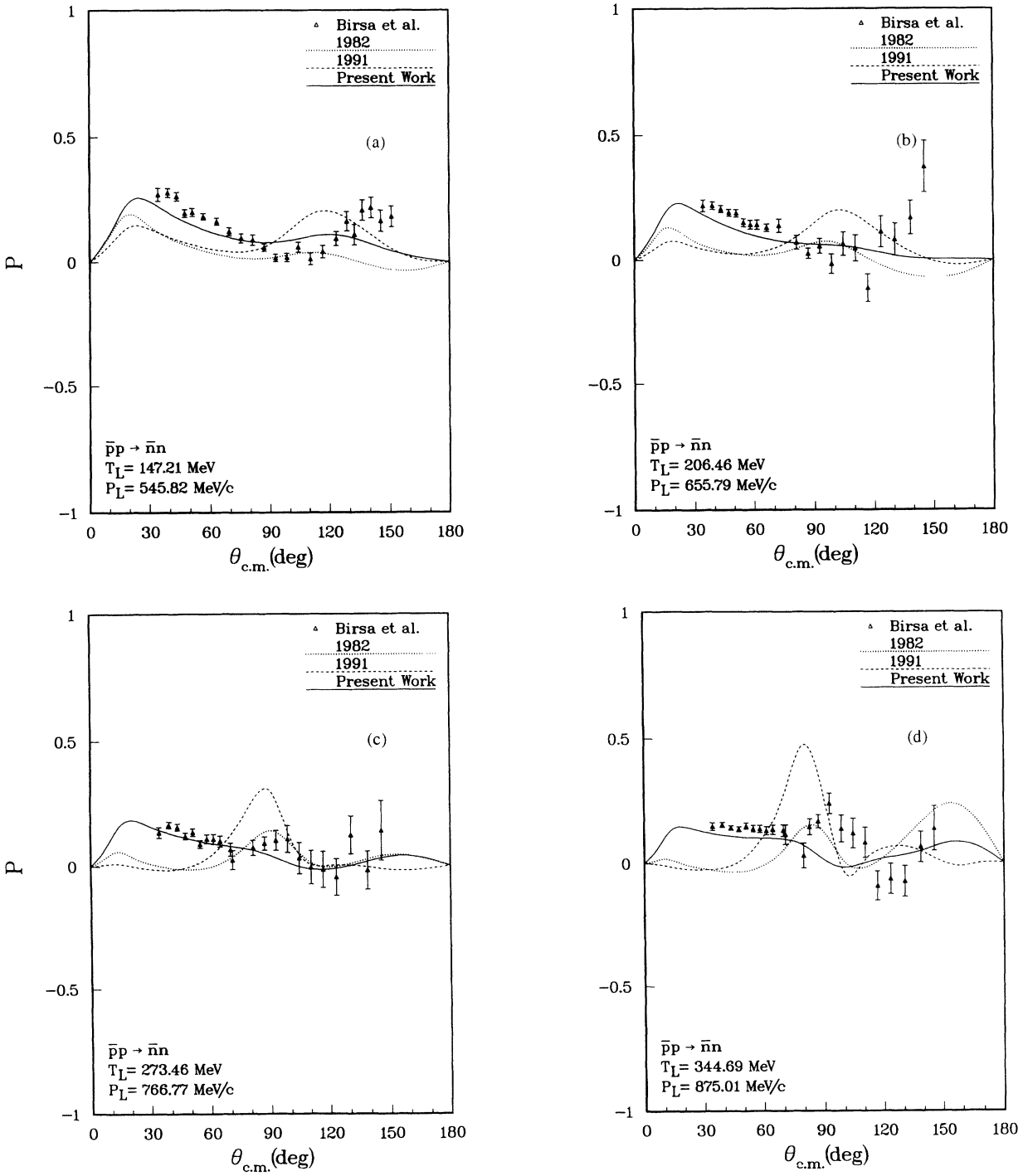

FIG. 6. Charge-exchange polarizations for different values of T_L. Curves are as in Fig. 2. Data are from Birsa *et al.* [34].

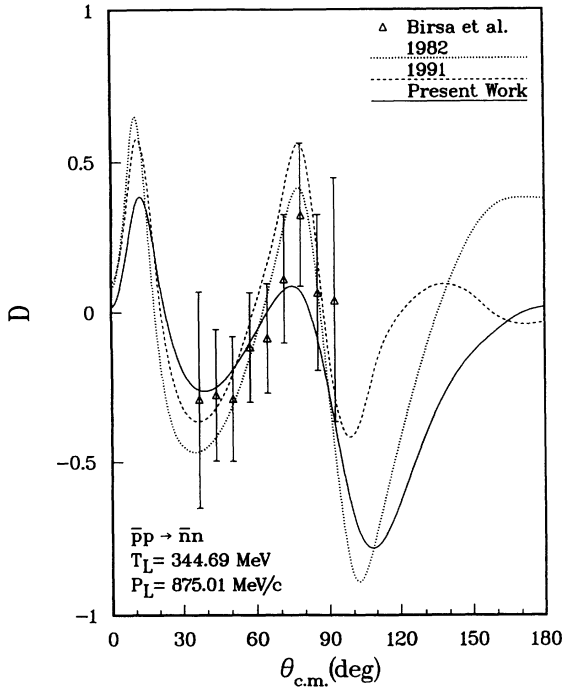

FIG. 7. Charge-exchange depolarization for $T_L = 344.7$ MeV. Curves are as in Fig. 2. Data are from Birsa *et al.* [35].

the test of isospin dependence. Our model agrees with experiments for the total as well as for the annihilation cross sections [42,43] (Fig. 9).

The results for the ρ parameter [18,28,41,44,45], the ratio of the real to imaginary parts of the forward scattering amplitude, are presented in Fig. 10. As before, our

TABLE II. Heights of the different components of the real potential at $r_3 = 0.20$ fm and $r_2 = 0.60$ fm determined by the fit to observables. All values are in MeV but the U_0^b components which are dimensionless.

Potentials	$T = 0$	$T = 1$
$U_0^a(r_3)$	7466.0	−5309.7
$U_0^a(r_2)$	−676.23	−1037.9
$U_0^b(r_2)$	0.837 24	0.075 88
$U_1^a(r_3)$	−1298.4	5193.7
$U_1^a(r_2)$	796.26	−1238.8
$U_1^b(r_2)$	−1.9259	−2.4216
$U_{LS}(r_2)$	701.14	−107.81
$U_T(r_2)$	237.55	188.57
$U_{SO2}(r_2)$	54.956	91.979

results agree with data but at low energies, as in other potential models, we are unable to reproduce the positive values obtained by Brückner *et al.* [41] and Linssen *et al.* [18].

D. The optical $N\bar{N}$ potential

The different components of the real and imaginary parts of our $N\bar{N}$ optical potential [Eqs. (2.1) and (A1)–(A18) and Tables II and III] are plotted in Figs. 11 and 12. It is interesting to observe the influence of the constraints given by the new and more accurate data on the SR behavior of the optical potential.

It is for distances below 0.7 fm that our real potential starts to deviate strongly from that of Ref. [1]. Singlet and triplet central potentials of both isospins are all at-

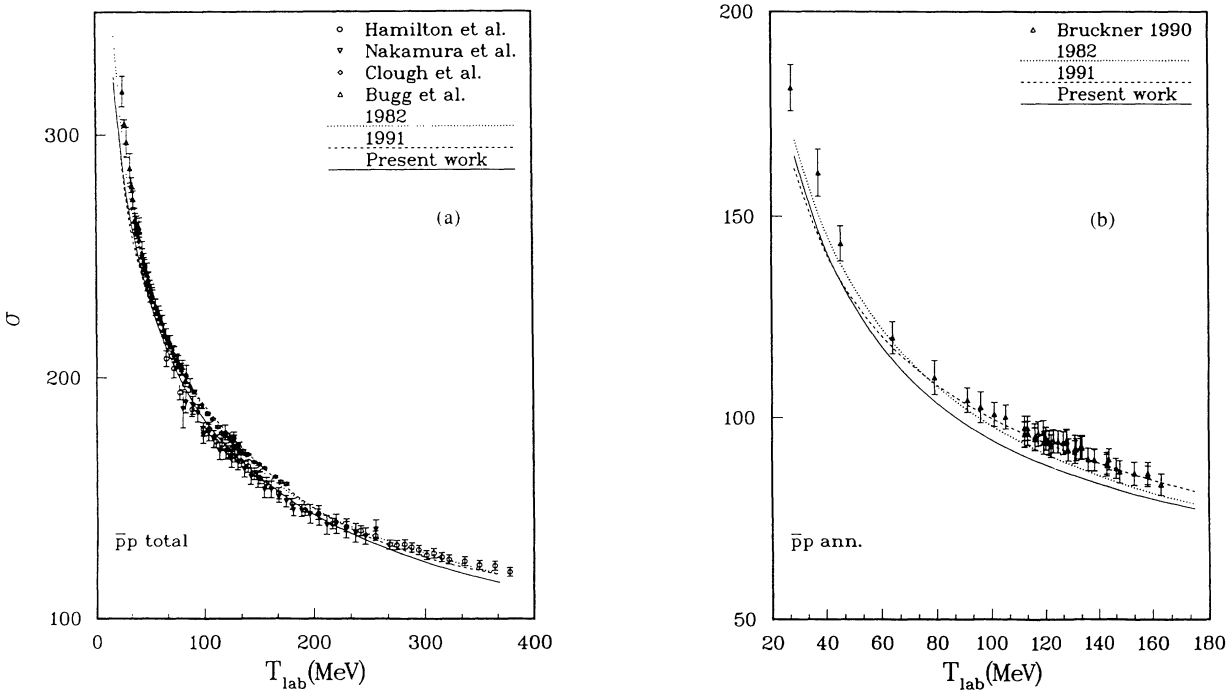

FIG. 8. Total and annihilation cross sections for the $\bar{p}p$ system. Curves are as in Fig. 2. Data are from Hamilton *et al.* [7], Nakamura *et al.* [36], Clough *et al.* [37], Bugg *et al.* [38], and Brückner *et al.* [39–41].

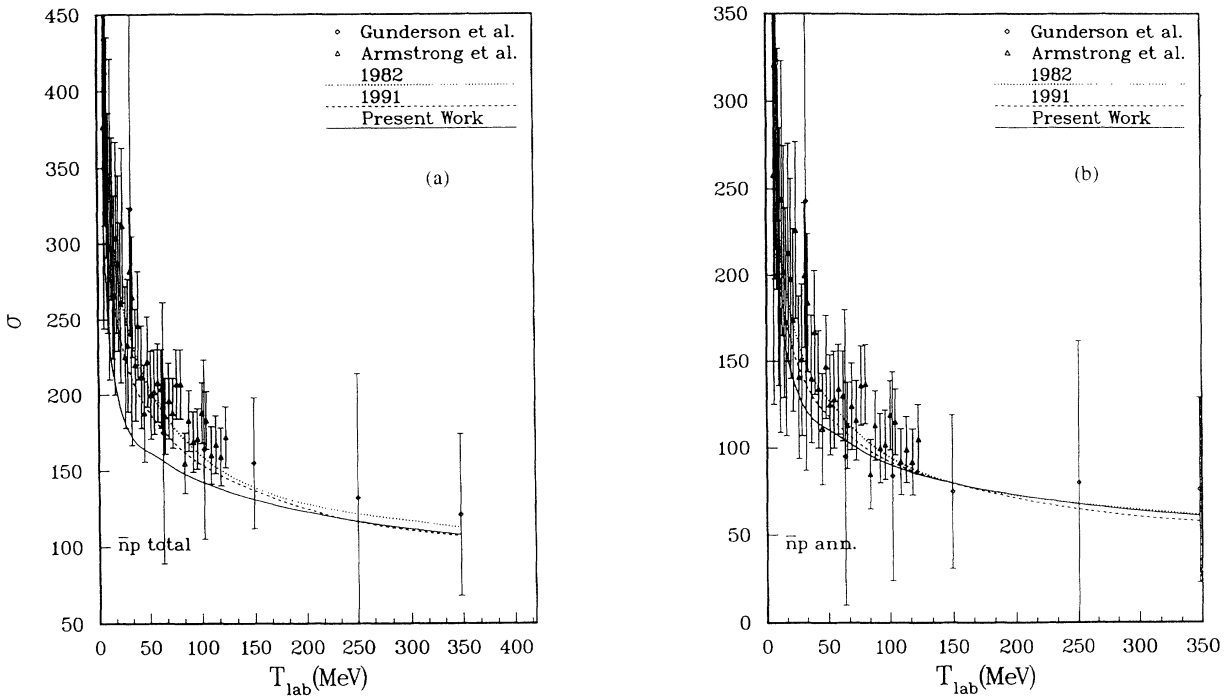

FIG. 9. Total and annihilation cross sections for the $\bar{n}p$ system. Curves are as in Fig. 2. Data are from Gunderson *et al.* [42] and Armstrong *et al.* [43].

tractive for $0.7 \leq r \leq 1$ fm. Here, in contrast to Ref. [1], the isoscalar singlet and isovector triplet central potentials become repulsive for $r \leq 0.5$ fm and the isovector central singlet stays attractive for $r \leq 0.7$ fm. The $T = 0$ LS component is more repulsive and the $T = 1$ less attractive. The tensor $T = 0$ potentials are repulsive and similar, while the $T = 1$ potential is now repulsive.

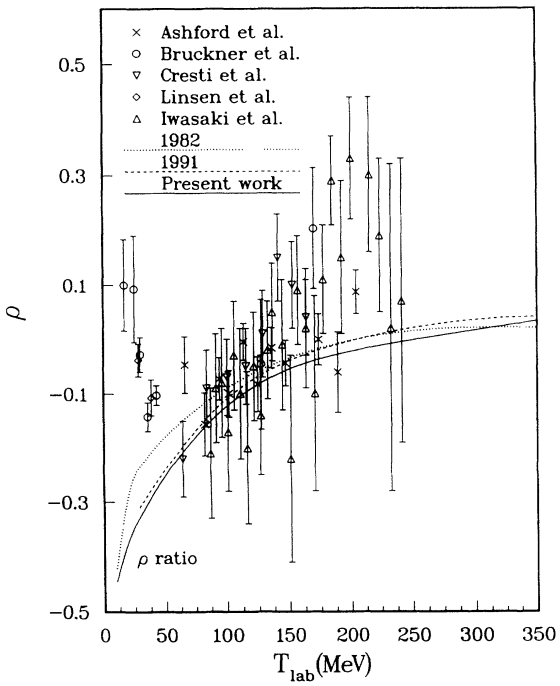

FIG. 10. Real to imaginary ratio ρ of the forward scattering amplitude for the $\bar{p}p$ system. Curves are as in Fig. 2. Data are from Linssen *et al.* [18], Cresti, Peruzzi, and Sartori [28], Brückner *et al.* [41], Iwasaki *et al.* [44], and Ashford *et al.* [45].

The isospin 0 and 1 singlet central imaginary potentials are much weaker than those of the 1982 solution [Fig. 12(a)]. This follows from the corresponding values of the g_i parameters given in Ref. [1] and in Table III. The isospin 0 and 1 triplet central components are similar [Fig. 12(b)]. The energy dependences are comparable, except for the isospin-1 triplet central imaginary potential. They are negligible in the 1982 version, but presently as strong as for the isospin-0 case. The spin-orbit components are much weaker and, as in 1982, very little isospin dependent [Fig. 12(c)]. The tensor potentials are also weaker with, however, a strong isospin dependence, as the $T = 0$ and $T = 1$ potentials have opposite signs.

E. Phase shifts

1. *Phases*

For completeness, in the Appendix, we recall the definition of the different phase parameters, η_L, δ_L, ϵ_J,

TABLE III. The parameters of the imaginary part $W_{N\bar{N}}$ of the absorptive potential.

	i	g_i	f_i (MeV^{-1})
$T = 0$	C	180.31	0.022 05
	SS	29.80	0.005 35
	LS	8.041	
	T	−6.077	
$T = 1$	C	63.67	0.050 37
	SS	10.55	0.058 05
	LS	7.467	
	T	8.838	

and α_J, expressing the S-matrix elements in the Livermore parametrization [46]. The phases are displayed in Figs. 13–17 for total angular momentum $J \leq 2$. We use the standard spectroscopic notation $^{2T+1}{}^{2S+1}L_J$ for a given partial wave characterized by its isospin T (0 or 1), spin S (0 or 1), angular momentum L, and total angular momentum J.

In general one can see an important isospin dependence. In contrast to the other $J = 0$ phases, the $^{13}P_0$ phase is positive at low energy and exhibits a quick rise to its maximum around 25 MeV and then becomes negative above 100 MeV [Fig. 13(a)]. We shall find later that this low energy behavior corresponds to the presence of a resonant state near threshold. Like the $^{13}P_0$, the $^{33}D_2$ phase also shows a resonant state [Fig. 15(a)]. The coupled $^3S_1$ phases are all negative and strongly absorbed (Fig. 16). In comparison with the phases obtained with the previous models [1,30], the $^{13}P_0$ phases are very similar and, as expected, as soon as the SR potentials start to act, i.e., above 50 MeV, the present D phases begin

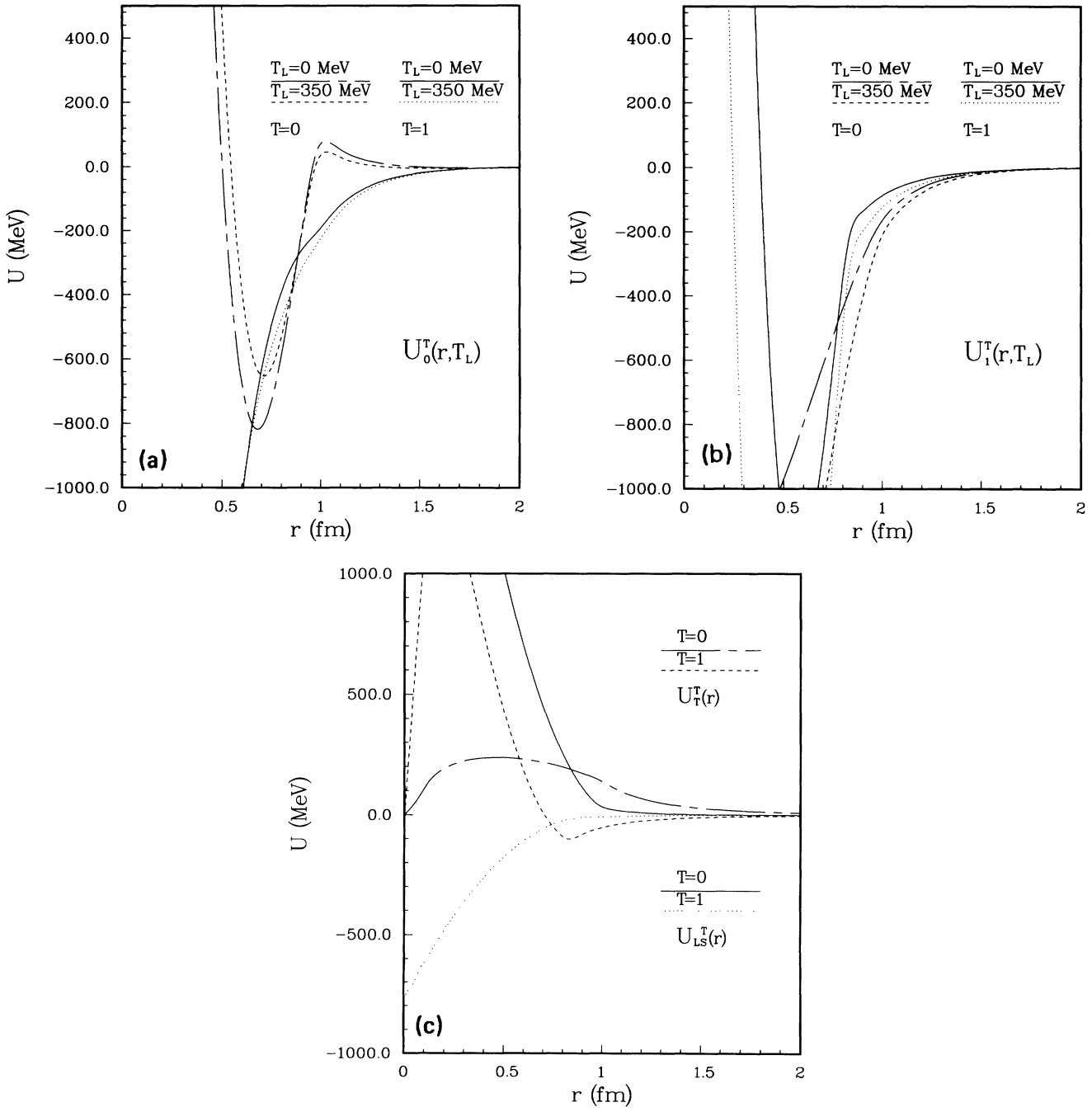

FIG. 11. Present work real potentials.

TABLE IV. The low energy parameters of the present work.

Wave	a_L	r_{0L}	P_L	Q_L
$^{11}S_0$	0.565 04 − i0.184 73	20.037 + i13.854	0.003 29 − i0.006 25	−0.000 03 − i0.000 03
$^{31}S_0$	0.836 35 − i0.906 54	1.5463 + i0.238 16	1.0510 − i0.352 39	0.789 05 − i1.0894
$^{13}S_1$	1.1878 − i0.602 56	0.797 81 − i1.5686	0.111 65 + i0.501 31	−0.288 09 − i0.087 57
$^{33}S_1$	−0.224 15 − i0.540 69	−19.580 − i10.804	0.005 82 − i0.001 35	0.000 02 − i0.000 03
$^{13}P_0$	−9.3315 − i4.5894	0.291 15 − i0.946 97	0.978 83 − i0.847 13	−0.439 71 + i0.469 63
$^{33}P_0$	2.7654 − i0.007 73	−4.9876 − i0.037 36	0.001 30 − i0.000 92	−0.000 41 + i0.000 02
$^{11}P_1$	−3.8478 − i1.8270	2.0853 − i2.5431	−0.056 83 − i0.089 23	0.015 554 + i0.002 27
$^{31}P_1$	0.852 39 − i0.565 66	−9.1362 − i15.996	−0.006 76 + i0.004 31	0.000 08 − i0.000 02
$^{13}P_1$	5.1377 − i0.041 09	−3.2986 − i0.043 07	−0.011 24 − i0.002 14	−0.004 10 + i0.000 36
$^{33}P_1$	−0.782 53 − i0.381 65	19.763 − i20.259	−0.007 76 − i0.002 84	0.000 05 − i0.000 03
$^{13}P_2$	−0.088 51 − i1.4724	1.0360 − i0.746 58	−1.4772 + i2.7843	−5.3497 − i0.112 92
$^{33}P_2$	−0.122 07 − i0.085 03	0.781 25 − i107.71	−0.000 23 − i0.000 27	0.000 00 + i0.000 00

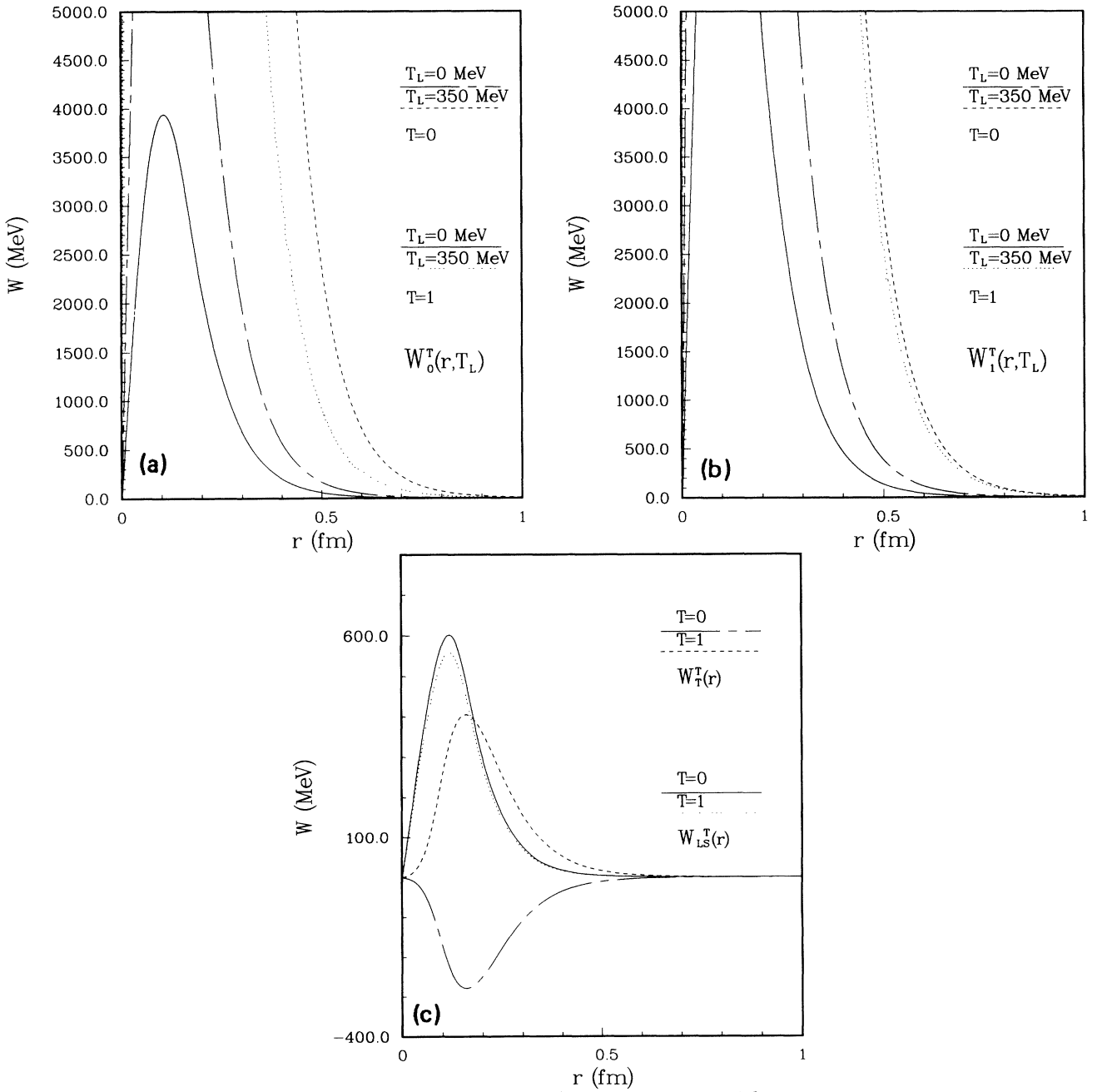

FIG. 12. As in Fig. 11 but for imaginary potentials.

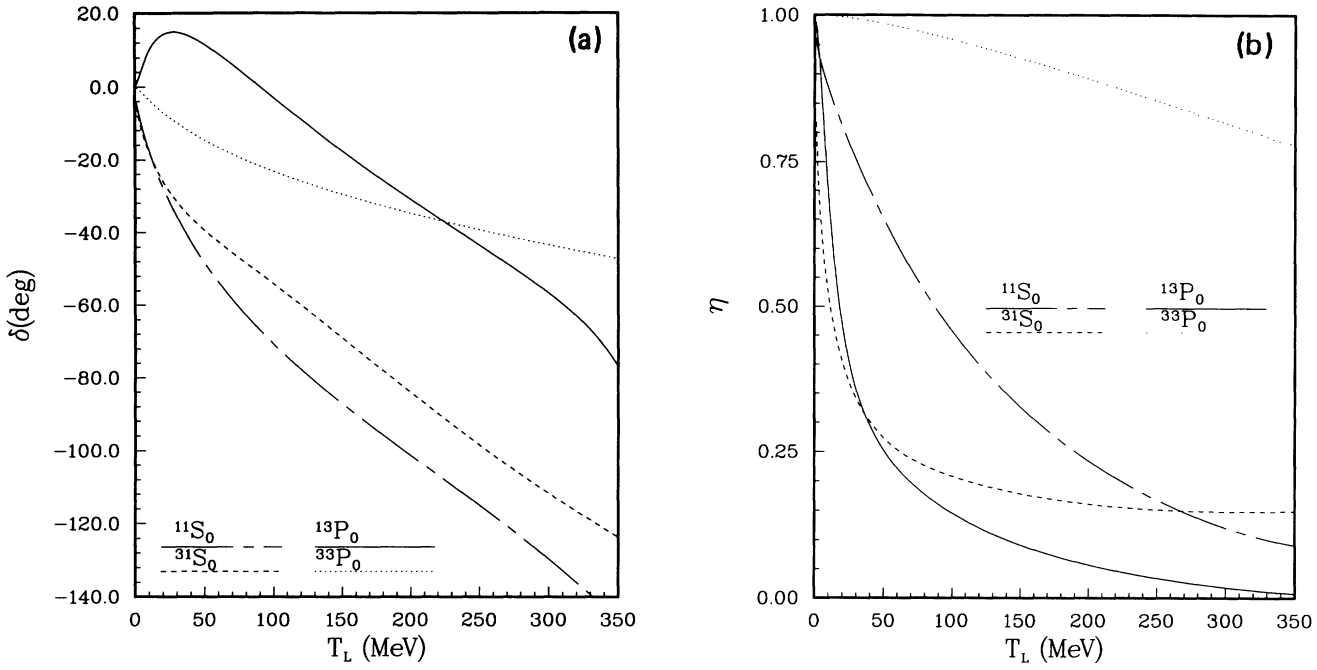

FIG. 13. Present work $J = 0$ phase parameters.

to be different. The $J = 3, 4$ phases, not plotted here, show very little model dependence and are almost elastic for $T_{\rm lab} < 200$ MeV. The absorption for the coupled $^3D_3$ phases appears, however, above 50 MeV and can be as important as for the uncoupled D phases.

2. *Low energy parameters*

In order to study the very low-energy behavior of the phases, we performed, for $0.01 \leq T_{\rm lab} \leq 10$ MeV, a least squares fit of the S and P phases without Coulomb force, using the effective range formula [Eq. (A22) of the Appendix]. In Table IV we give the results, for the scattering length a_L, the effective range r_{0L}, and the parameters P_L and Q_L. We have checked that the scattering lengths are very close to the values obtained by solving the Schrödinger equation at zero energy. As the low energy behavior of the S and P phases is different from those of our previous models [1,30], the low energy pa-

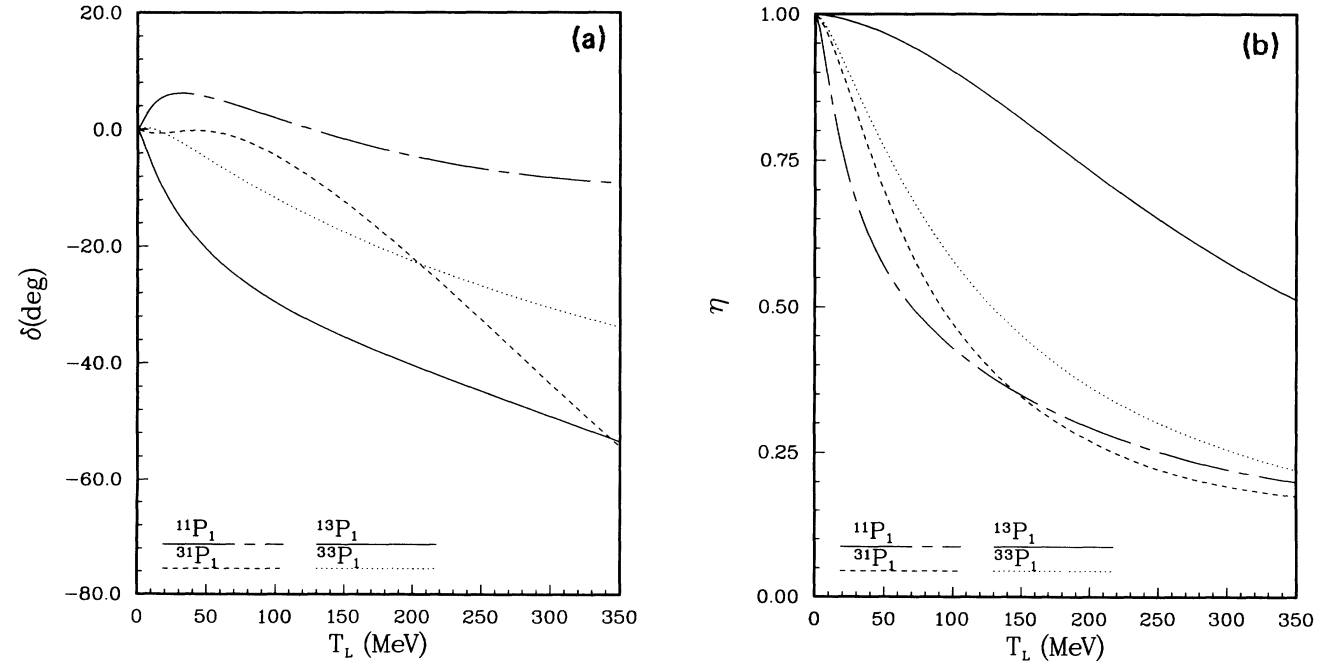

FIG. 14. Present work uncoupled $J = 1$ phase parameters.

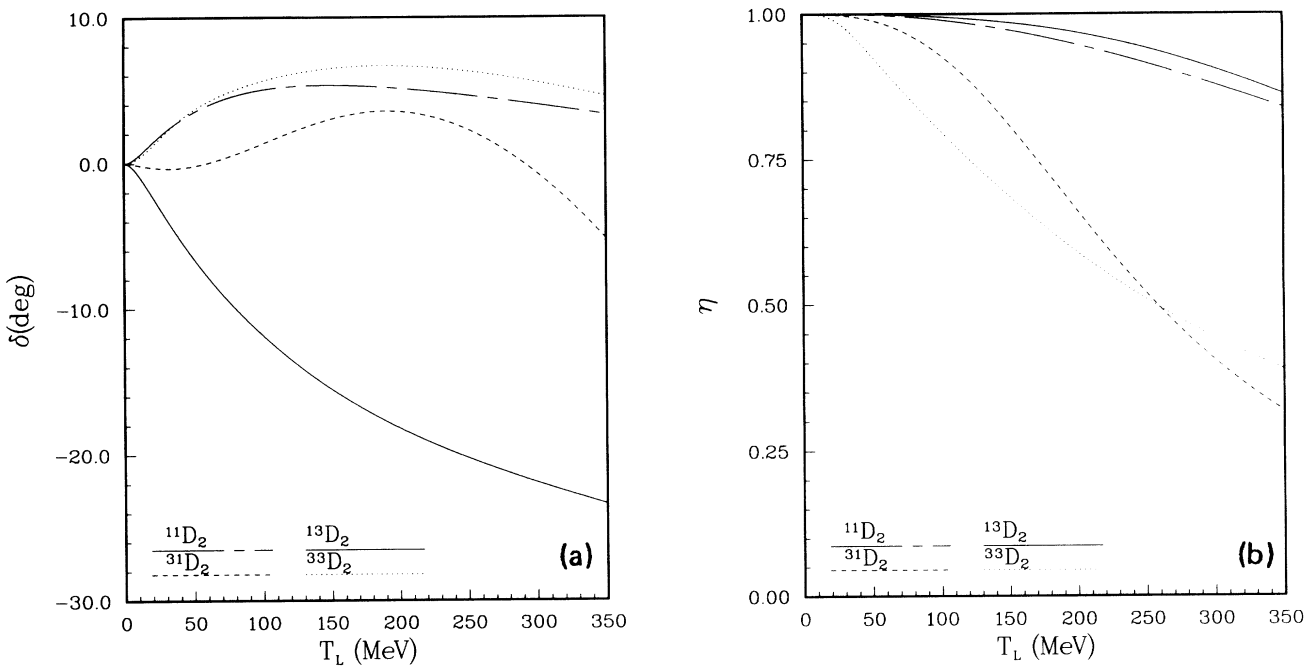

FIG. 15. Present work uncoupled $J = 2$ phase parameters.

rameters are different except for the $^{33}P_0$ and $^{13}P_1$ waves. The large values of the r_{0L} parameters for the $^{11}S_0$, $^{33}S_1$, $^{31}P_1$, and $^{33}P_1$ waves comes from the strong energy dependence of these particular phases. The large value for $a_L(^{13}P_0)$ is due to the presence of the threshold resonance in this wave, as we shall see next.

The scattering wave functions of our optical potentials have also been calculated and can be used to take into account initial state interaction in processes such as strangeness production from $\bar{p}p$, or $\bar{p}p$ annihilation into two pions [47].

F. Resonances and bound states

Following the method of Ref. [48] we have calculated the spectrum of the $N\bar{N}$ resonances of the present model. Let us recall that, in potential scattering, for a given partial wave, the S matrix can be written in terms of the Jost function $F(k)$ as

$$S(k) = \frac{F(-k)}{F(k)} \tag{3.1}$$

with

$$k^2 = m\frac{T_{\rm lab}}{2} = mE, \tag{3.2}$$

where m is the nucleon mass and E the c.m. relative energy.

We have searched for poles of the S matrix in the complex momentum plane lying reasonably close to the real axis, i.e., $-m_\pi < \mathrm{Im}k < 0$, where m_π is the pion mass. These resonances correspond to the zeros of $F(k)$ in the domain $\mathrm{Im}k < 0$, $\mathrm{Re}k > 0$. As explained in the Appendix of Ref. [48], an analytic continuation is needed for the calculation of the Jost function in the region $\mathrm{Im}k < -m_\pi/2$. If the imaginary part of the potential is set to 0 many resonances are found, as expected from the very attractive nature of the real potential. With the complete potential these states become wide and many of them now have $\mathrm{Im}k < -m_\pi$.

Table V gives a list of the complex momenta of the poles with $|\mathrm{Im}k| < m_\pi$ together with the mass and width of the corresponding resonances. In comparison with Tables I and IV of Ref. [48] we can see the following. (i) Fewer resonances are found here, four instead of six previously, and they are in general narrower. Three of them occur in the same states: $^{13}P_0$, $^{33}D_2$, and $^{33}F_3$. The previous $^{31}P_1$,$^{33}(F\text{-}H)_4$, and $^{33}G_4$ stats are absent but a new one in the $^{33}(D\text{-}G)_3$ state appears. This is a consequence of a weaker $T = 1$ imaginary triplet potential at low energy. (ii) All resonances occur in the triplet isotriplet states except for the $^3P_0$. If the imaginary potential is zero, there are as many resonant triplet states in

TABLE V. Resonances of the present model.

$^{2T+1}2S+1L_J$	$^{13}P_0$	$^{33}D_2$	$^{33}F_3$	$^{33}(D\text{-}G)_3$
Rek (fm^{-1})	0.24	0.70	1.39	1.03
Imk (fm^{-1})	−0.26	−0.17	−0.22	−0.28
Mass (MeV)	1876	1896	1953	1917
Width (MeV)	10.4	19.9	50.8	47.8

TABLE VI. Binding energy in MeV of the possible $^{2T+1\,2S+1}L_J$ bound states of the present model.

$^{13}P_0$	$^{13}P_1$	$^{33}P_1$	$^{13}(S\text{-}D)_1$	$^{33}(S\text{-}D)_1$	$^{13}(P\text{-}F)_2$	$^{33}(P\text{-}F)_2$
$-238 - i48$	$-67 - i66$	$-29 - i4.7$	$-151 - i45$	$-114 - i0.4$	$-320 - i3.2$	$-70 - i4.2$

both isospins. Switching it on, the isosinglet states pick up a large width because of the large $T = 0$ component at low energy [Fig. 12(b)]. As was shown in Ref. [48] one does not expect a loop in the Argand diagram; however a sharp rise of the phase can be seen in the Argand plots for the $^{13}P_0$, $^{33}D_2$, and $^{33}F_3$ states in Figs. 18–20.

The absorptive part of our optical potential has a linear energy dependence [see Eq. (A15)]. This is not suitable for the search for bound state far from threshold. For this purpose we account for the energy dependence of $W_{N\bar{N}}(r, 2E)$ by an exponential $\exp(\alpha E)$, α being fitted to reproduce the linear dependence in the range

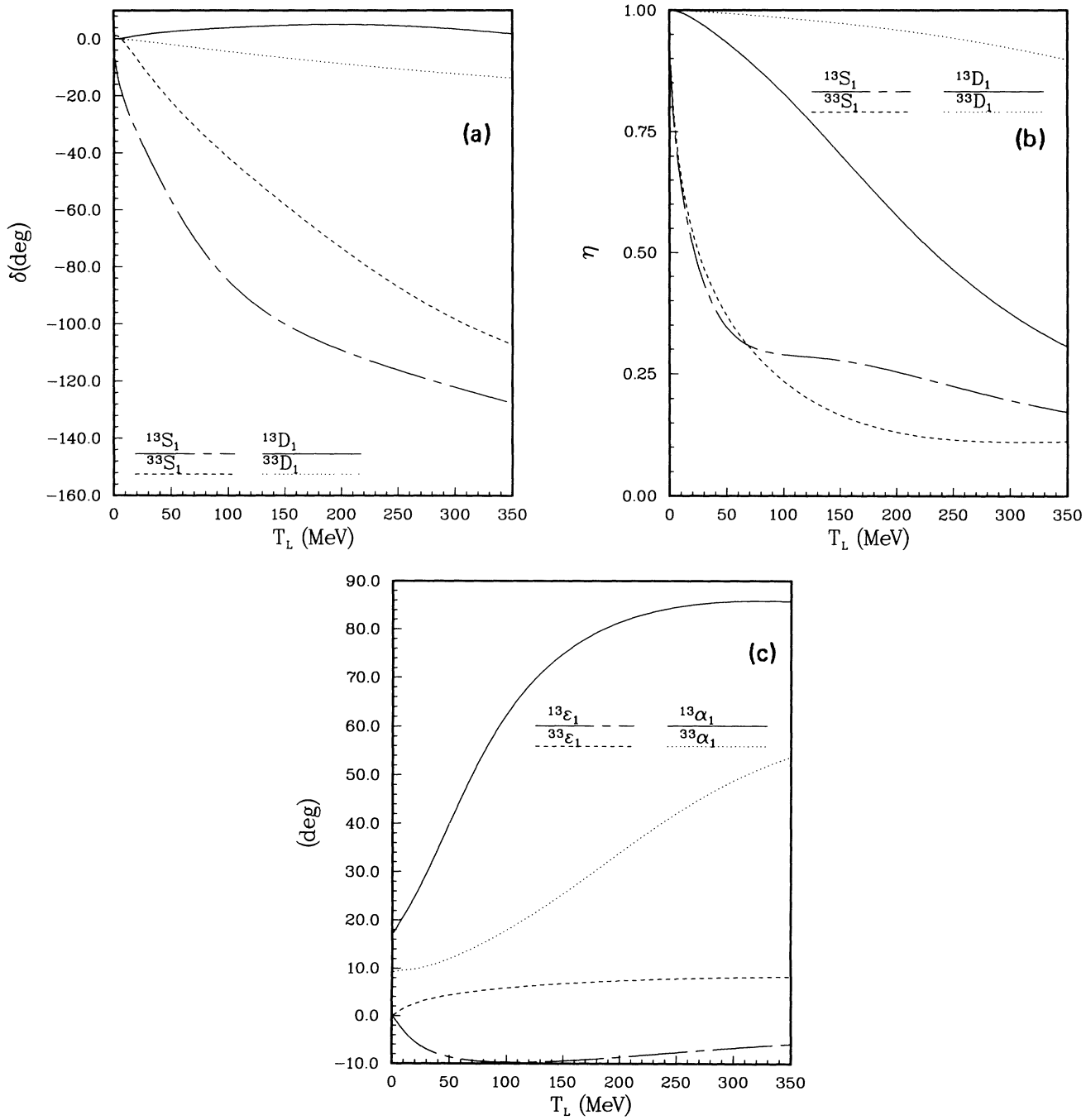

FIG. 16. Present work coupled $J = 1$ phase parameters.

$0 \leq E \leq 300$ MeV. Bound states have Re$k < 0$ and Im$k > 0$. If the imaginary part is set to 0, there are many bound states, again all in triplet states. If the imaginary potential is turned on, some of these states acquire a large width or have Re$k > 0$. Table VI gives the list of the remaining bound states. It is interesting to note that, if the $AX(1565)$ is to be interpreted as a $^{13}(P-F)_2$ bound state of the $N\bar{N}$ system as advocated in Ref. [49], we predict such a bound state at the right energy.

IV. SUMMARY AND CONCLUSIONS

In this work, we pursue further our investigation program on the $N\bar{N}$ interaction initiated in 1982. We con-

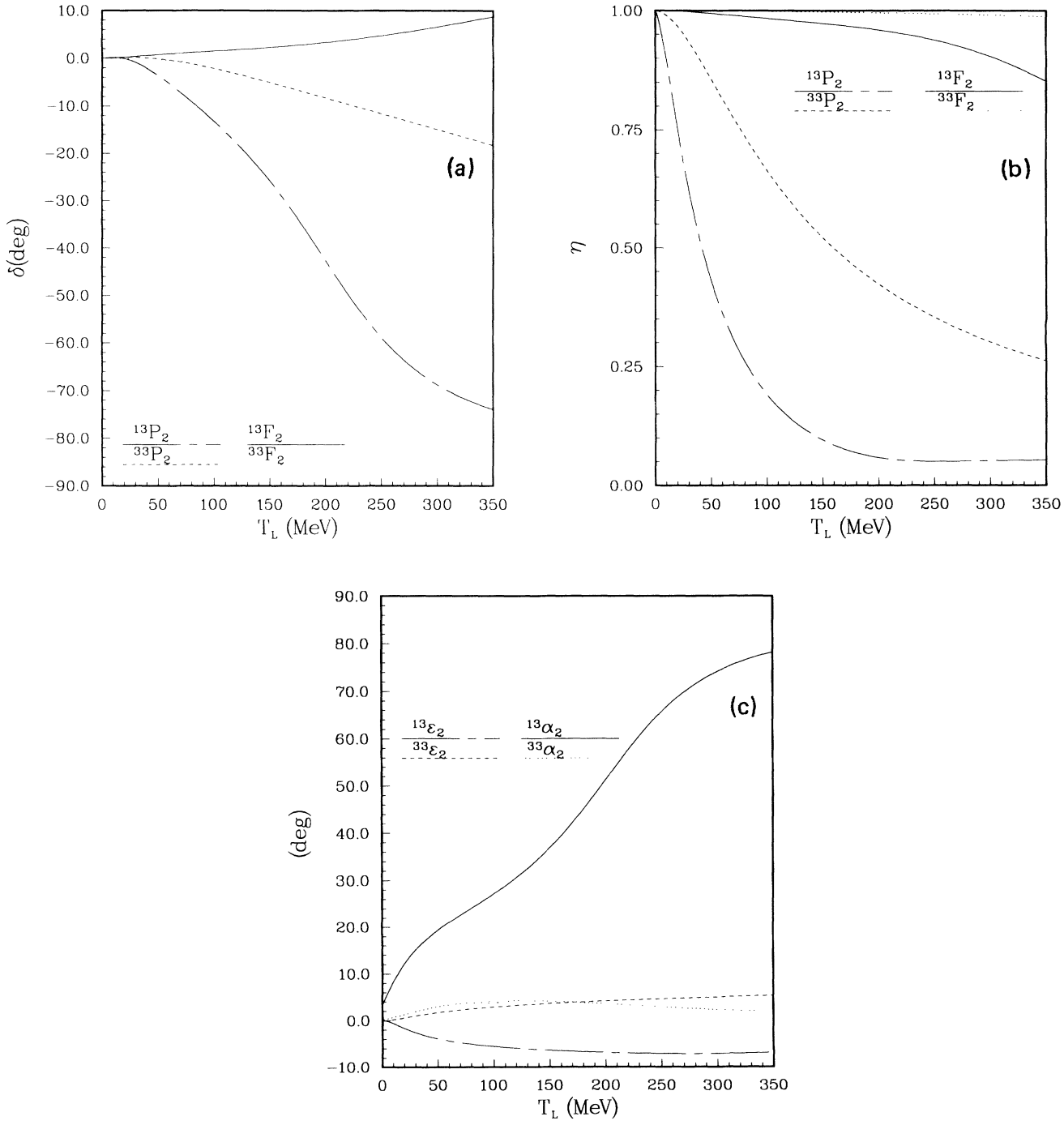

FIG. 17. As in Fig. 16 but for the coupled $J = 2$ phase parameters.

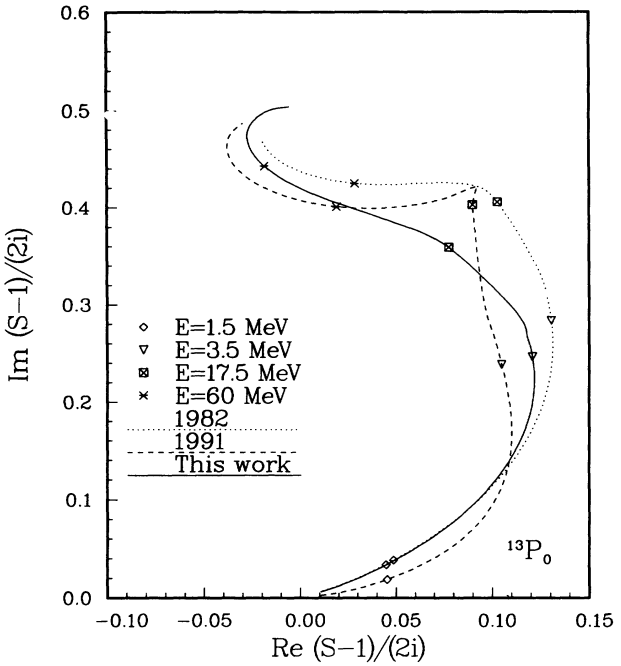

FIG. 18. Comparison of the present work $^{13}P_0$ Argand diagram, continuous solid line, to those of our earlier models. The 1982 amplitude of Ref. [1] is represented by a dotted line and that of 1991, Ref. [30], by a dashed line.

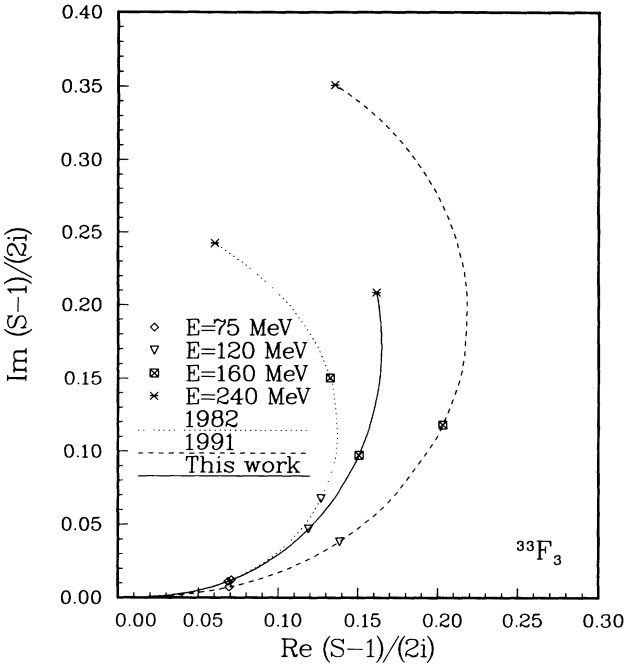

FIG. 20. As in Fig. 2 but for the $^{33}F_3$ amplitude.

template the possibility of combining well established theoretical inputs (i.e., the LR+MR parts of the interaction as derived from meson exchanges) with the wealth of existing experimental data in order to get an accurate phenomenological representation of the SR part of the interaction. The underlying idea is similar to that followed in the construction of the Paris NN potential; however, with more degrees of freedom here because of the presence of annihilation. We start with a parametrization of the SR potential, for the real as well as the imaginary parts, which contains 15 parameters for each isospin state. From a superficial overlook, this number might appear too large, but having in mind that, from general principles, the description of the $N\bar{N}$ interaction requires the knowledge of ten real functions with two variables (nonlocal potentials), for each isospin state, we consider this parametrization as minimal. On the other hand, as discussed in the text, our fitting procedure permits us to distinguish the important parameters describing the bulk properties from those allowing just a fine tuning of the fit.

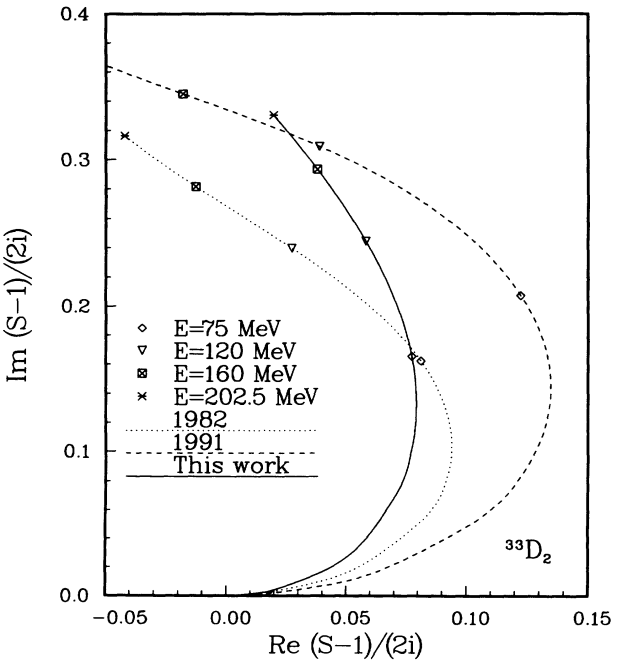

FIG. 19. As in Fig. 2 but for the $^{33}D_2$ amplitude.

From the total existing data set (3800 data), some (168) are clearly inconsistent with others. We performed the determination of the parameters on the remaining set (3632 data). A quantitative measure of the quality of the fit can be provided by the value of χ^2/data. The fit gives 3.87. If some further less clearly inconsistent data (337) are dropped, the calculated χ^2/data is 2.46. We did not try to perform a best fit to this latter restricted set of data which would give lower χ^2/data. Of course, because of the presence of inconsistent data the calculated χ^2/data for the total set data is large, 4.8. The figures show clearly the improvement of the model between 1982 and 1994 due to the constraints provided by the data of new observables like elastic polarization and charge-exchange cross sections and analyzing power. Paradoxically, the recent measurements on elastic cross sections are not so constraining. Perhaps the present version of our model is not definite, and could be improved

with further experimental data.

It should be stressed that the improvement is obtained by modifying only the short-range part of the interaction, essentially for $r < 0.7$ fm. This means that the hope of pinning down the SR part from experimental observables once reliable LR+MR parts are given is not illusory. Since the validity of the LR+MR parts of our model is well founded on theoretical grounds and well supported by experimental data, the properties of our SR part can provide valuable hints in the elaboration of a deeper theoretical model for the short-range part of the $N\bar{N}$ interaction.

ACKNOWLEDGMENTS

We thank B. Moussallam for helpful discussions and for providing us his numerical code to calculate the resonances and bound states of the present optical $N\bar{N}$ potential. Division de Physique Théorique is Unité de Recherche des Universités Paris 11 et Paris 6 Associée au CNRS.

APPENDIX

1. The real potential

For completeness, we give here the full expression of the real potential. For the two isospin values $T = 1$ and $T = 0$, the potential is expressed in terms of the usual nonrelativistic invariants:

$$\begin{aligned} U_{N\bar{N}}(\vec{r}, T_{\rm lab}) = {} & U_0(r, T_{\rm lab})\Omega_0 + U_1(r, T_{\rm lab})\Omega_1 \\ & + U_{LS}(r)\Omega_{LS} + U_T(r)\Omega_T \\ & + U_{\rm SO2}(r)\Omega_{\rm SO2}, \end{aligned} \tag{A1}$$

where

$$\begin{aligned} \Omega_0 &= (1 - \vec{\sigma}_1 \cdot \vec{\sigma}_2)/4, \\ \Omega_1 &= (3 + \vec{\sigma}_1 \cdot \vec{\sigma}_2)/4, \\ \Omega_{LS} &= \vec{L} \cdot \vec{S}, \\ \Omega_T &= 3\frac{\vec{\sigma}_1 \cdot \vec{r}\vec{\sigma}_2 \cdot \vec{r}}{r^2} - \vec{\sigma}_1 \cdot \vec{\sigma}_2, \\ \Omega_{\rm SO2} &= \tfrac{1}{2}(\vec{\sigma}_1 \cdot \vec{L}\vec{\sigma}_2 \cdot \vec{L} + \vec{\sigma}_2 \cdot \vec{L}\vec{\sigma}_1 \cdot \vec{L}). \end{aligned} \tag{A2}$$

Here the nonlocality of the central component is accounted for by an energy dependence which is taken to be linear. It replaces the p^2 dependence used in [1]. Explicitly, the central singlet, U_0, and central triplet, U_1, potentials are given by

$$U(r, T_{\rm lab}) = U^a(r) + T_{\rm lab}U^b(r). \tag{A3}$$

For $r > r_c$, the potential is given by the G-parity transform of the theoretical NN Paris potential [50,51]. As in Ref. [51], for the ω exchange ($m_\omega = 782.7$ MeV), we use $g_\omega^2/4\pi = 11.75$. For the shorter range A_1 exchange ($m_{A_1} = 1100$ MeV), we take $g_{A_1}^2/4\pi = 10.4$; this gives a more attractive isospin-0 central singlet potential in the 1 fm range.

For $r < r_c$, the phenomenological potentials are expanded in powers of r:

$$U(r) = a_3r^2 + a_2r^2 + a_1r + a_0 \tag{A4}$$

for U_0^a and U_1^a, and

$$U(r) = b_2r^2 + b_1r + b_0 \tag{A5}$$

for $U_{0,1}^b, U_{LS}, U_T$, and $U_{\rm SO2}$.

The parameters $a_i (i = 0, 1, 2, 3)$ and $b_i (i = 0, 1, 2)$ are determined by the following: (i) Matching to the theoretical potential at $r_0 = r_c$ and $r_1 = r_c + \Delta r$, $\Delta = 0.15$ fm. For all isospin-0 potentials, $r_c = 1$ fm. For all isospin-1 components, $r_c = 0.84$ fm except for U_0^a where $r_c = 1$ fm. (ii) Choosing a phenomenological height at $r_2 = 0.60$ fm, and also at $r_3 = 0.20$ fm for $U_{0,1}^a$.

The values of the different potential at r_2 and r_3, determined by the fit to the data, are given in Table II.

In solving the Schrödinger equation, we have regularized the tensor potential $U_T(r)$, at small r, with

$$F(r) = \frac{(pr)^2}{1 + (pr)^2} \tag{A6}$$

and $p = 10$ fm^{-1}.

2. The imaginary potential

As stated in the text, the imaginary part $W_{N\bar{N}}$ of the optical potential can be obtained from the unitarity condition applied to the $N\bar{N}$ amplitude $\langle n_2\bar{p}_2|A|n_1\bar{p}_1\rangle$ (see Fig. 21). This reads

$$\mathrm{Im}A = \frac{|\vec{a}|}{16\pi^2\sqrt{s}} \int d\Omega_a \langle n_2\bar{p}_2|A^+|ab\rangle\langle ab|A|n_1\bar{p}_1\rangle, \tag{A7}$$

where $\vec{a}$ is the c.m. system three-momentum of the two intermediate bosons,

$$|\vec{a}|^2 = [s - (\mu_a + \mu_b)^2][s - (\mu_a - \mu_b)^2]/4s, \tag{A8}$$

with $\mu_{a,b}$ the masses of the bosons a, b and $s = (p_1 + n_1)^2$.

In the approximation where one retains only the nucleon pole in the amplitude $\langle ab|A|\bar{p}_1n_1\rangle$, Eq. (A7) becomes

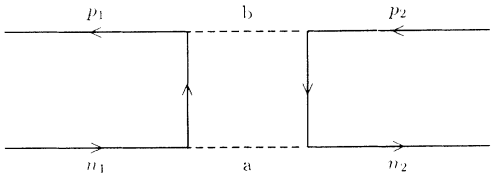

FIG. 21. $N\bar{N}$ annihilation diagram into two mesons.

$$\mathrm{Im}A = \frac{|\vec{a}|}{16\pi^2\sqrt{s}} \int d\Omega_a \bar{v}(p_1) r_1^b \frac{\gamma_1 \cdot (n_1 - a) + M}{(n_1 - a)^2 - M^2} r_1^a u(n_1) \times \bar{u}(n_2) r_2^a \frac{\gamma_2 \cdot (n_2 - a) + M}{(n_2 - a)^2 - M^2} r_2^b v(p_2), \quad \text{(A9)}$$

where u and v represents Dirac spinors for particle and antiparticle, $\gamma_{1,2}$ are Dirac matrices, and M is the nucleon mass. The coupling operators $r_{1,2}^{a,b}$ will have different expressions according to the nature of the boson a or b. For instance, if the boson a is scalar, $r_1^a = r_2^a = g_a$ (coupling constant), and if it is pseudoscalar, $r_{1,2}^a = \tilde{g}_a \gamma_{1,2}^5$, and so on.

Expanding the Dirac spinors and matrices in terms of the Pauli matrices, one can show that

$$\mathrm{Im}A = \sum_i I_i(s,t) \tilde{\Omega}_i, \quad \text{(A10)}$$

where $\tilde{\Omega}_i$ are the invariants of Eq. (A2), but written in momentum space, and the coefficients $I_i(s,t)$ are integrals which can be expressed [16] in terms of

$$I_0(s,t) = \int d\Omega_a \frac{1}{[(n_1 - a)^2 - M^2][(n_2 - a)^2 - M^2]}. \quad \text{(A11)}$$

The latter can be evaluated as

$$I_0(s,t) = \frac{2\pi}{|\vec{a}|^2} \int_{4m^2}^{+\infty} \frac{dt'}{\sqrt{t'(t' - 4m^2)}(t' - t)}, \quad \text{(A12)}$$

where t is the momentum transfer $t = (n_1 - n_2)^2$, and

$$4m^2 = 4M^2 + \frac{\mu_a^2 \mu_b^2}{|\vec{a}|^2}. \quad \text{(A13)}$$

The presence of the nucleon and antinucleon propagators in Eq. (A9) shows clearly that ImA contains the baryon-antibaryon exchange in the crossed channel, and one can anticipate that the annihilation diagrams are effective only for t large and positive (which correspond to small distances in coordinate space) as explicitly shown by Eq. (A12). Moreover, ImA is energy dependent; actually, for the energy domain of interest in this work, the energy dependence of ImA is very weak for all spin components and moderate for the central ones. In other words, the coefficients I_i in Eq. (A10) are functions of t only, except for $i = C$ and SS, where the energy dependence can be taken to be linear. The I_i's can be calculated explicitly in terms of masses and coupling constants. However, as mentioned above, ImA is of "short range," and as we have adopted to describe the short-range part of the real potential phenomenologically, there is no need to retain the exact expressions for the I_i's. We approximate them by effective phenomenological couplings (with a linear energy dependence for the central and spin-spin components).

The imaginary part $\tilde{W}_{N\bar{N}}$ of the optical potential, in momentum space, can be derived in the same way as in Ref. [50], giving

$$\tilde{W}_{N\bar{N}} \sim \mathrm{Im}A. \quad \text{(A14)}$$

By Fourier transforming $\tilde{W}_{N\bar{N}}(s,t)$ one would get, in configuration space, a nonlocal potential. However, as the energy dependence of $\tilde{W}_{N\bar{N}}$ is rather weak, we keep it fixed in the Fourier transform. In this case we obtain for each isospin state ($T = 0, 1$)

$$W_{N\bar{N}}(\vec{r}, T_{\mathrm{lab}}) = \Big[g_C(1 + f_C T_{\mathrm{lab}}) + g_{SS}(1 + f_{SS} T_{\mathrm{lab}}) \vec{\sigma}_1 \cdot \vec{\sigma}_2 + g_T \Omega_T + \frac{g_{LS}}{4m^2} \Omega_{LS} \frac{1}{r} \frac{d}{dr} \Big] \frac{K_0(2mr)}{r}, \quad \text{(A15)}$$

where the modified Bessel function $K_0(2mr)$ comes from the Fourier transform of I_0, i.e.,

$$\tilde{I}_0(r) = \frac{1}{2} \int_{4m^2}^{\infty} dt' \frac{e^{-\sqrt{t'}r}}{\sqrt{t'(t' - 4m^2)}} = K_0(2mr). \quad \text{(A16)}$$

In Eq. (A16) m is taken to be very close to the nucleon mass, viz., $m = 940$ MeV. The values of the parameters g_i and f_i determined by the fitting procedure are given in Table III.

Here again, in solving the Schrödinger equation, to avoid the singular behavior at $r = 0$, we have regularized the central and spin-spin potentials of Eq. (A15) with

$$G(r) = (1 - e^{-2mr})^4, \quad \text{(A17)}$$

and the spin-orbit and tensor potentials with

$$H(r) = (1 - e^{-2mr})^7. \quad \text{(A18)}$$

3. S matrix in terms of phase shifts and effective range formula

Following the Livermore parametrization [46] to express the S-matrix elements in terms of phase shifts we write, for uncoupled states,

$$S_J(T_{\mathrm{lab}}) = \eta_J e^{2i\delta_J} \quad \text{(A19)}$$

and for coupled states

$$S_{L,L'}(T_{\mathrm{lab}}) = \begin{pmatrix} S_{J-1,J-1}(T_{\mathrm{lab}}) & S_{J-1,J+1}(T_{\mathrm{lab}}) \\ S_{J+1,J-1}(T_{\mathrm{lab}}) & S_{J+1,J+1}(T_{\mathrm{lab}}) \end{pmatrix}, \quad \text{(A20)}$$

with

$$\begin{aligned} S_{J-1,J-1}(T_{\mathrm{lab}}) &= \eta_{J-1} \cos(2\epsilon_J) e^{2i\delta_{J-1}}, \\ S_{J-1,J+1}(T_{\mathrm{lab}}) &= i \sin(2\epsilon_J) e^{i(\delta_{J-1} + \delta_{J+1} + \alpha_J)}, \\ S_{J+1,J-1}(T_{\mathrm{lab}}) &= S_{J-1,J+1}(T_{\mathrm{lab}}), \\ S_{J+1,J+1}(T_{\mathrm{lab}}) &= \eta_{J+1} \cos(2\epsilon_J) e^{2i\delta_{J+1}}. \end{aligned} \quad \text{(A21)}$$

The phase parameters $\eta_L, \delta_L, \epsilon_J$, and α_J are all $T_{\rm lab}$ dependent.

The effective range formula used to calculate the low energy parameters is

$$k^{2L+1}\cot\left(\delta_L - \frac{i}{2}\ln\eta_L\right) = -\frac{1}{a_L} + \tfrac{1}{2}r_{0L}k^2 - P_L r_{0L}^3 k^4 + Q_L r_{0L}^5 k^6. \quad \text{(A22)}$$

[1] J. Côté, M. Lacombe, B. Loiseau, B. Moussallam, and R. Vinh Mau, Phys. Rev. Lett. **48**, 1319 (1982).
[2] B. Conforto, G. Fidecaro, H. Steiner, R. Bizzarri, P. Guidoni, F. Marcelja, G. Brantti, E. Castelli, M. Ceschia, and M. Sessa, Nuovo Cimento A **54**, 441 (1968).
[3] D. Spencer and D. N. Edwards, Nucl. Phys. **B19**, 501 (1970).
[4] H. Kohno *et al.*, Nucl. Phys. **B41**, 485 (1972).
[5] E. Eisenhandler *et al.*, Nucl. Phys. **B113**, 1 (1976).
[6] M. Alston-Garnjost, R. P. Hamilton, R. W. Kenney, D. L. Pollard, R. D. Tripp, H. Nicholson, and D. M. Lazarus, Phys. Rev. Lett. **43**, 1901 (1979).
[7] R. P. Hamilton, T. P. Pun, R. D. Tripp, D. M. Lazarus, and H. Nicholson, Phys. Rev. Lett. **44**, 1182 (1980).
[8] V. Chaloupka *et al.*, Phys. Lett. **61B**, 487 (1976).
[9] T. Kamae *et al.*, Phys. Rev. Lett. **44**, 1439 (1980).
[10] T. Oshugi *et al.*, Nuovo Cimento A **17**, 456 (1973).
[11] M. Kimura *et al.*, in *Proceedings of the Fourth European Symposium on $N\bar{N}$ Interactions* (CNRS, Paris, 1979), p. 539.
[12] R. P. Hamilton, T. P. Pun, R. D. Tripp, H. Nicholson, and D. M. Lazarus, Phys. Rev. Lett. **44**, 1179 (1980).
[13] T. Tsuboyama, Y. Kubota, F. Sai, S. Sakamoto, and S. S. Yamamoto, Phys. Rev. D **28**, 2135 (1983).
[14] R. Bizzari, B. Conforto, G. C. Gialanella, P. Guidoni, F. Marcelja, E. Castelli, M. Ceschia, and M. Sessa, Nuovo Cimento A **54**, 456 (1968).
[15] M. Lacombe, B. Loiseau, J-M. Richard, R. Vinh Mau, P. Pires, and R. de Tourreil, Phys. Rev. D **12**, 1495 (1975).
[16] R. Vinh Mau, in *Proceedings of the Fourth European Symposium on $N\bar{N}$ Interactions* [11], p. 463; B. Moussallam, Ph.D. thesis, Universite Paris VI, 1980 (unpublished); Nucl. Phys. **A407**, 413 (1983); R. Vinh Mau, in *Hadron Structure in Nuclear Physics (Bloomington, Indiana)*, Proceedings of the 1983 Indiana University Nuclear Physics Workshop on Manifestations of Hadron Substructure in Nuclear Physics, edited by W-Y. P. Hwang and M. H. Macfarlane, AIP Conf. Proc. No. 110 (AIP, New York, 1983), p. 187; in *Medium Energy Nucleon and Antinucleon Scattering*, edited by H. V. von Geramb, Lecture Notes in Physics Vol. 243 (Springer-Verlag, Berlin, 1985), pp. 3–23.
[17] C. B. Dover, Nucl. Phys. **A558**, 721c (1993).
[18] L. Linssen *et al.*, Nucl. Phys. **A469**, 726 (1987).
[19] P. Schiavon *et al.*, Nucl. Phys. **A505**, 595 (1989).
[20] W. Brückner *et al.*, Phys. Lett. **166B**, 113 (1986); Z. Phys. A **339**, 367 (1991).
[21] F. Perrot-Kunne *et al.*, Phys. Lett. B **261**, 188 (1991).
[22] R. A. Kunne *et al.*, Nucl. Phys. **B323**, 1 (1989).
[23] R. Bertini *et al.*, Phys. Lett. B **228**, 531 (1989).
[24] T. Kageyama, T. Fujii, K. Nakamura, F. Sai, S. Sakamoto, S. Sato, T. Takahashi, T. Tanimori, and S. S. Yamamoto, Phys. Rev. D **35**, 2655 (1985).
[25] H. Iwasaki *et al.*, Phys. Lett. **103B**, 247 (1981).
[26] H. Kaseno *et al.*, Nuovo Cimento A **43**, 119 (1978).
[27] S. Sakamoto, T. Hashimoto, F. Sai, and S. S. Yamamoto, Nucl. Phys. **B195**, 1 (1982).
[28] M. Cresti, L. Peruzzo, and G. Sartori, Phys. Lett. **132B**, 209 (1983).
[29] M. G. Albrow *et al.*, Nucl. Phys. **B137**, 247 (1981).
[30] M. Pignone, M. Lacombe, B. Loiseau, and R. Vinh Mau, Phys. Rev. Lett. **67**, 2423 (1991).
[31] K. Nakamura, T. Fujii, T. Kageyama, F. Sai, S. Sakamoto, S. Sato, T. Takahashi, T. Tanimori, and S. S. Yamamoto, Phys. Rev. Lett. **53**, 885 (1984).
[32] W. Brückner *et al.*, Phys. Lett. **169B**, 302 (1986).
[33] R. Birsa *et al.*, Phys. Lett. B **246**, 267 (1990).
[34] R. Birsa *et al.*, Phys. Lett. B **273**, 533 (1991).
[35] R. Birsa *et al.*, Phys. Lett. B **302**, 517 (1993).
[36] K. Nakamura *et al.*, Phys. Rev. D **29**, 349 (1984).
[37] A. S. Clough *et al.*, Phys. Lett. **146B**, 299 (1984).
[38] D. V. Bugg *et al.*, Phys. Lett. B **194**, 563 (1987).
[39] W. Brückner *et al.*, Phys. Lett. B **197**, 463 (1987).
[40] W. Brückner *et al.*, Z. Phys. A **335**, 217 (1990).
[41] W. Brückner *et al.*, Phys. Lett. **158B**, 180 (1985).
[42] B. Gunderson, J. Learned, J. Mapp, and D. D. Reeder, Phys. Rev. D **23**, 587 (1981).
[43] T. Armstrong *et al.*, Phys. Rev. D **36**, 659 (1987).
[44] H. Iwasaki *et al.*, Nucl. Phys. **A433**, 580 (1985).
[45] V. Ashford, M. E. Sainio, M. Sakitt, J. Skelly, R. Debbe, W. Finckinger, R. Marino, and D. K. Robinson, Phys. Rev. Lett. **54**, 518 (1985).
[46] M. H. MacGregor, R. A. Arndt, and P. M. Wright, Phys. Rev. **169**, 1149 (1968).
[47] P. LaFrance, B. Loiseau, and R. Vinh Mau, Phys. Lett. B **214**, 317 (1988); P. LaFrance and B. Loiseau, Nucl. Phys. **A528**, 557 (1991).
[48] M. Lacombe, B. Loiseau, B. Moussallam, and R. Vinh Mau, Phys. Rev. C **29**, 1800 (1984).
[49] C. B. Dover, T. Gutsche, and A. Faessler, Phys. Rev. C **43**, 379 (1991).
[50] W. N. Cottingham, M. Lacombe, B. Loiseau, J-M. Richard, and R. Vinh Mau, Phys. Rev. D **8**, 800 (1973).
[51] M. Lacombe, B. Loiseau, J-M. Richard, R. Vinh Mau, J. Côté, P. Pirés, and R. de Tourreil, Phys. Rev. C **21**, 861 (1980).